J. Fluid Mech. (2023), *vol*. 968, A30, doi:10.1017/jfm.2023.553

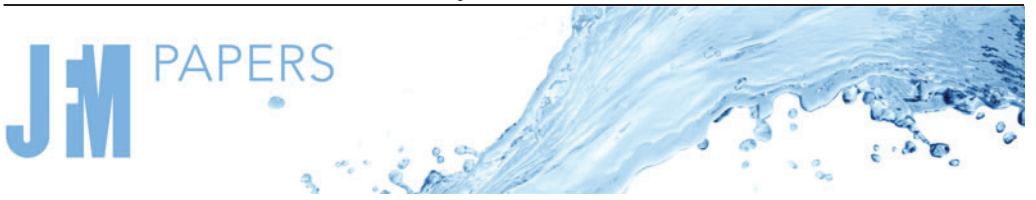

Static and dynamic stability of pendant drops

Fei Zhang[1] **and Xinping Zhou**[1,2,†]

[1]School of Mechanical Science and Engineering, Huazhong University of Science and Technology, Wuhan 430074, PR China

[2]State Key Laboratory of Intelligent Manufacturing Equipment and Technology, Huazhong University of Science and Technology, Wuhan 430074, PR China

(Received 21 March 2023; revised 6 June 2023; accepted 4 July 2023)

Despite the widespread occurrence of pendant drops in nature, there is still a lack of combined studies on their dynamic and static stability. This study focuses on the dynamic and static stability of elongated drops with either a free or pinned contact line on a plane. We first examine static stability for both axisymmetric and non-axisymmetric perturbations subject to volume or pressure constraints. The stability limits for volume and pressure disturbances (axisymmetric) correspond to the maximum volume and pressure of the drops, respectively. Drops with free contact lines are marginally stable to non-axisymmetric perturbations because of their horizontal translational invariance, whereas pinned drops are stable. The linear dynamic stability is then investigated numerically through a boundary element model, restricted to volume disturbances. Results show that when the stability limit is reached, the first zonal mode has a zero frequency, suggesting that the thresholds for static and dynamic stability are essentially equivalent. Furthermore, natural frequencies experience sharp changes as the stability limit is approached. Another zero frequency mode associated with the horizontal motion of the centre of mass is also revealed by the numerical results, reflecting the horizontal translational invariance of drops with free contact lines. Finally, the frequency spectrum modified by gravity is explored, resulting in the identification of five gravity-induced frequency shift patterns. The frequency shifts break the spectral degeneracy for hemispherical drops with free contact lines, leading to various spectral orderings according to polar and azimuthal wavenumbers.

Key words: drops, capillary flows, boundary integral methods

1. Introduction

Stability of capillary surfaces is an important topic in the hydrodynamics of multiphase flow. Capillary surfaces dominated by surface tension may suffer from a variety of classical

† Email address for correspondence: xpzhou08@hust.edu.cn

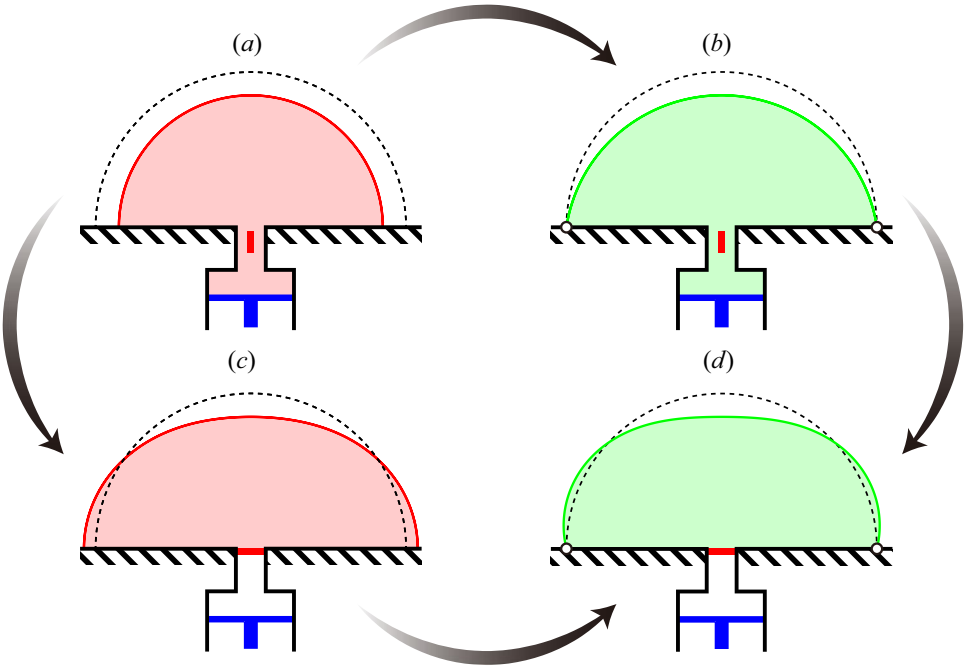

Figure 1. Schematic diagrams of (*a*,*b*) pressure and (*c*,*d*) volume disturbances of partially wetting drops, with (*a*,*c*) free and (*b*,*d*) pinned CLs. The solid and dashed lines indicate the disturbance and the base state, respectively. The blue T-shaped piston is to keep the liquid pressure constant, and the red bars placed vertically and horizontally indicate the opening and closing of the valve, respectively, to switch between preserving-pressure and preserving-volume constraints. The stabilising effects of CL pinning and the volume constraint are indicated by the horizontal and vertical arrows, respectively, with stabilisation along the direction of the arrows (see also Bostwick & Steen 2015, figure 10).

instabilities, such as the Plateau–Rayleigh instability (Rayleigh 1878; Haefner *et al.* 2015; Pham, Perrard & Le Doudic 2020), the Rayleigh–Taylor instability (Daly 1969; Scase & Hill 2018) and the Faraday instability (Kumar & Tuckerman 1994; Kumar 1996). As essential tools in the study of capillary instability (Michael 1981; Bostwick & Steen 2015), static stability analysis predicts the onset of instability, and dynamic stability analysis gives the growth rate of instability or the vibrational properties in forms of natural frequencies, damping factors and mode shapes. The stability theory serves as an underlying framework for an overall understanding of capillary instability.

Partially wetting drops on a plane are typical examples of stability analysis of capillary surfaces and have continued to receive special attention in recent years (Bostwick & Steen 2014, 2015, 2016; Chang *et al.* 2015; Steen, Chang & Bostwick 2019; Montanero & Ponce-Torres 2020; Ding & Bostwick 2022*a*,*b*; McCraney *et al.* 2022). Prior to performing static and dynamic stability analysis, in addition to the base state (i.e. the equilibrium shape), two other conditions are required: (i) whether the contact line (CL) is pinned or free, and (ii) whether the liquid bulk is subject to a volume or pressure constraint (figure 1). The free (pinned) CL condition is to keep the contact angle (CL) fixed under disturbances. Similarly, volume (pressure) disturbances preserve the volume (pressure) of the base state. The switching between the above pressure and volume constraints might be achieved by the on–off of the valve in the experiment, as shown in figure 1.

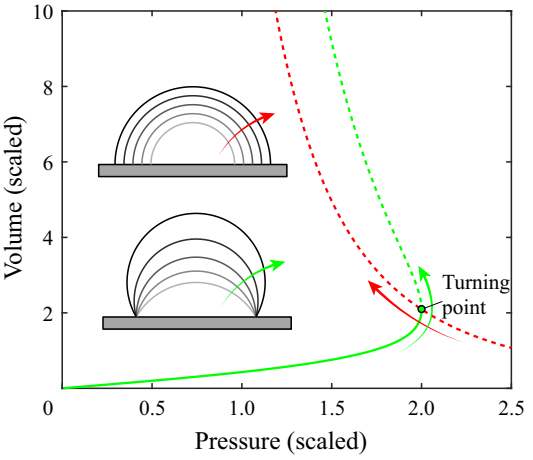

Figure 2. Volume–pressure diagrams of gravity-free drops with free CLs ($\alpha = 90^\circ$, red line) and pinned CLs ($R = 1$, green line). Drops with free CLs and hydrophobic ($\alpha > 90^\circ$) drops with pinned CLs are p-unstable (dashed line), while the hydrophilic ($\alpha < 90^\circ$) drops with pinned CLs are p-stable (solid line). The hemispherical drop with a pinned CL (green point) is marginally p-stable. Drops with either free or pinned CLs are always v-stable.

Static stability is illustrated briefly by gravity-free sessile drops (see also Bostwick & Steen 2015). Noting that the sessile and pendant drops without gravity are identical, the following stability analysis also holds true for gravity-free pendant drops. Based on the Young–Laplace equation, the equilibrium shape is a spherical cap determined by the drop volume V and contact angle α. After scaling, the Laplace pressure P and volume V of the liquid are related by $V = 8\pi P^{-3}(2 + \cos\alpha)(1 - \cos\alpha)^2/3$, where $P = 2\sin\alpha/R$, with R being the CL radius. Obviously, we have $\mathrm{d}P/\mathrm{d}V < 0$ for drops with free CLs (see the red line in figure 2), indicating that all equilibria are unstable to pressure disturbances (called p-unstable) (Bostwick & Steen 2015); for pinned CLs, the hydrophilic drops ($\alpha < 90^\circ$) are p-stable due to the stabilisation of CL pinning, while the hydrophobic drops ($\alpha > 90^\circ$) are still p-unstable. Thus the hemispherical drop ($\alpha = 90^\circ$) with a pinned CL corresponding to a vertical turning point (TP) is marginally p-stable, consistent with the Poincaré–Maddocks (PM) theory (Maddocks 1987; Lowry & Steen 1995). By contrast, all equilibria are stable to volume disturbances (called v-stable) due to the stabilisation of the volume constraint (Bostwick & Steen 2015). The above stability results can be interpreted physically as follows: under pressure disturbances, the derivative $\mathrm{d}P/\mathrm{d}V > 0$ means that an increase in the drop volume leads to an increase in the pressure, which expels the liquid and returns the volume to its initial state, whereas the opposite occurs for $\mathrm{d}P/\mathrm{d}V < 0$, thus giving instability (Bostwick & Steen 2015). However, this explanation does not account for the volume-preserving drops; they are stable because the configuration of the spherical cap on a plane has minimum surface energy (Marinov 2012). Both the pinned CL and volume constraint have a stabilising effect on static stability, as shown in figure 1.

Regarding dynamic stability, the seminal works of Rayleigh (1879) and Lamb (1932) used linear stability analysis to obtain the natural frequencies λ of a spherical inviscid drop:

$$\lambda^2_{[k,l]} = k\,(k-1)\,(k+2)\,, \quad k, l = 0, 1, \ldots, \quad l \leqslant k, \tag{1.1}$$

where k and l are the polar and azimuthal wavenumbers, respectively. The mode shapes are the spherical harmonics Y_k^l, which together with the degenerate frequencies (1.1) are called the Rayleigh–Lamb (RL) spectrum. For the spherical drop, there are $k = 0$ and $k = 1$ zero frequency modes, which reflect the conservation of volume and the symmetry of translational invariance, respectively (Bostwick & Steen 2009). Another noteworthy property of (1.1) is the spectral degeneracy of the RL spectrum, i.e. all modes with the same k have the same frequency. This spectral degeneracy can be broken by the external flow (Feng 1992), the drop rotation (Busse 1984) and the external fields (Feng & Beard 1991; Shi & Apfel 1995). The inclusion of an eccentric bubble in drops also eliminates the degeneracy (Sumanasekara & Bhattacharya 2017), while the concentric geometry ensures this degeneracy (Bhattacharya 2016). Interestingly, finite-amplitude oscillations and viscosity do not break the spectral degeneracy of spherical drops (Trinh, Zwern & Wang 1982; Tsamopoulos & Brown 1983; Wang, Anilkumar & Lee 1996).

The RL spectrum is modified for gravity-free sessile drops (Chang *et al.* 2013). As the solid surface constrains the drop, only the $k + l =$ even modes are preserved due to the non-penetration condition. For hemispherical drops with free CLs (called free semi-drops), the modes still satisfy the RL spectrum (1.1) with $k + l =$ even, thereby maintaining the spectral degeneracy and resulting in a zero frequency $[1, 1]$ mode that relates to the horizontal displacement of the centre of mass. Lyubimov, Lyubimova & Shklyaev (2004, 2006) found that the frequencies of free semi-drops are raised by CL pinning, with greater shifts for larger l. As a consequence, the spectral degeneracy is broken and the $[1, 1]$ mode has a non-zero frequency. Bostwick & Steen (2014) found that varying contact angle also breaks the spectral degeneracy, obeying that the larger l, the smaller the frequency for hydrophilic drops, and the opposite holds for hydrophobic drops. Accordingly, Steen *et al.* (2019) introduced the periodic tables of modes to characterise the above spectral orderings. Sharma & Wilson (2021) presented a fully analytical solution based on a toroidal analysis for drops with pinned CLs. In these studies, only volume disturbances are allowed. Recently, Ding & Bostwick (2022*b*) studied the dynamic stability of spherical cap drops for pressure disturbances.

Gravity plays a crucial role in the equilibrium and stability of partially wetting drops, which are elongated (pendant) or flattened (sessile) depending on the direction of gravity. The equilibria and static stability of sessile and pendant drops have been studied extensively (Padday 1971; Padday & Pitt 1972, 1973; Pitts 1974; Concus & Finn 1979; Finn 1986; Del Rıo & Neumann 1997; Sumesh & Govindarajan 2010; Pozrikidis 2012; Gulec *et al.* 2019). For equilibrium shapes, there are generally no closed-form solutions (Padday 1971; Finn 1986), but asymptotic solutions exist for some limiting cases (Yariv 2022). The stability of pendant drops is of particular concern compared to sessile drops because pendant drops may be v-unstable while sessile drops are always v-stable (Padday & Pitt 1973; Pitts 1974). This instability is closely related to the pinch-off phenomenon and drop detachment from a ceiling (Schulkes 1994; Henderson, Pritchard & Smolka 1997). The PM theory (Maddocks 1987; Lowry & Steen 1995) can deal with static stability for axisymmetric perturbations, indicating that the stability limit for volume (pressure) disturbances corresponds to the maximum volume (pressure) of the drop (see also Padday & Pitt 1973) (figure 2). For non-axisymmetric perturbations, the boundary parameter comparison approach (Myshkis *et al.* 1987; Zhang & Zhou 2020) is usually preferred to avoid solving a series of intractable eigenvalue problems (Myshkis *et al.* 1987; Bostwick & Steen 2015) for static stability.

Stable drops exhibit natural oscillations that reflect their dynamic stability. Many experiments and numerical simulations have investigated the effects of gravity on the frequency spectrum, where frequency prediction models are developed based on the modified RL spectrum (Yoshiyasu, Matsuda & Takaki 1996; Perez *et al.* 1999; Parkinson & Phan 2018), and analogies to harmonic oscillators (Celestini & Kofman 2006; Sakakeeny & Ling 2020, 2021; Sakakeeny *et al.* 2021) and one-dimensional waves (Noblin, Buguin & Brochard-Wyart 2004; Temperton, Smith & Sharp 2015). These works analysed the vibrational processes to extract the natural frequencies. An alternative is to solve a functional eigenvalue problem governing the linear dynamics of drops (Strani & Sabetta 1984; Myshkis *et al.* 1987; Bostwick & Steen 2014). This approach is accurate and efficient, but difficult to solve for drops of more general shape (Gañán & Barrero 1990; Gañán 1991). To investigate drops with arbitrary shapes, numerical methods for solving the eigenvalue problem are necessary (Siekmann & Schilling 1989; Ebrahimian, Noorian & Haddadpour 2013, 2015). Recently, Zhang, Zhou & Ding (2023) applied a boundary element (BE) model to gravity-flattened sessile drops, and found a complicated dependence of the frequency spectrum on gravity. However, a systematic understanding of the effect of gravity on the spectrum is still lacking for pendant drops with opposite gravity. In contrast to sessile drops, gravity destabilises pendant drops, leading to downward frequency shifts and capillary instability (Basaran 1992; Basaran & DePaoli 1994; Schulkes 1994). It is unclear if the downward frequency shifts are still maintained over a wider parameter domain. In addition, how static stability and dynamic stability are related for pendant drops is also an important issue. It is known that the Plateau limit of a capillary cylinder can be recovered from the dynamic stability with the growth rate being zero (Rayleigh 1879; Bostwick & Steen 2015). One can expect that the static stability of pendant drops can also be recovered from their dynamic stability, which gives us a different perspective on static stability.

In light of the above, this study will consider both the static and dynamic stability of pendant drops. Static stability is analysed first by the PM theory (Maddocks 1987) and the boundary parameter comparison approach (Myshkis *et al.* 1987) for axisymmetric and non-axisymmetric perturbations, respectively, and then dynamic stability is investigated numerically by the BE model (Zhang *et al.* 2023) that can deal with drops of arbitrary shape. The relation between static stability and dynamic stability is illustrated by the BE results of stability limits. Finally, we study the effects of gravity on the frequency spectrum and present some interesting consequences, such as zero frequency modes, breaking of spectral degeneracy, and spectral ordering due to gravity.

2. Mathematical formulation

In this section, we first give the governing equations of the base state for static and dynamic stability, then perform static stability analysis for both axisymmetric and non-axisymmetric perturbations, and finally write the functional eigenvalue problem of dynamic stability with a brief description of the mode classification of the BE model results.

2.1. *Equilibrium shapes of pendant drops*

Consider a pendant drop suspended from a plane as shown in figure 3, whose equilibrium interface is governed by the (dimensionless) Young–Laplace equation (see e.g. Padday

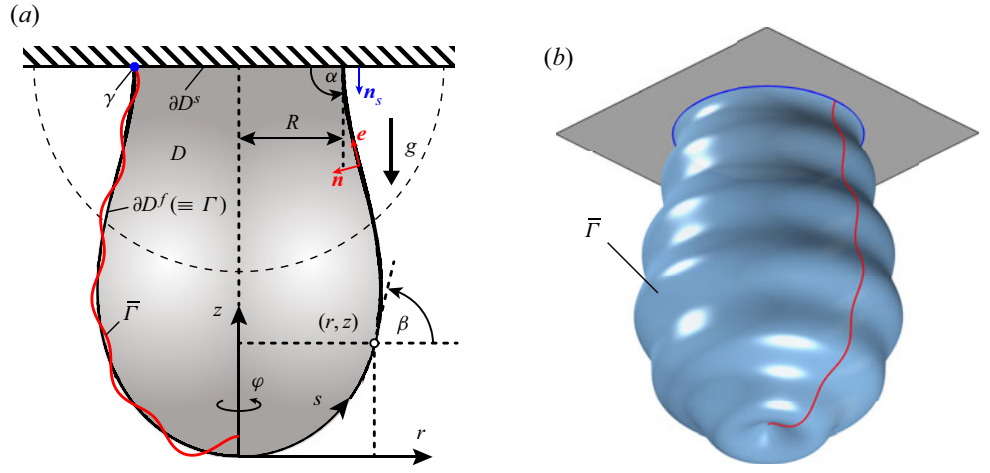

Figure 3. (*a*) Schematic diagram of a pendant drop suspended from a plane under gravity g, and (*b*) the rendered perturbed surface $\bar{\Gamma}$. For comparison, a gravity-free drop (dashed line) of the same volume is drawn.

1971; Del Río & Neumann 1997):

$$\left.\begin{aligned} \frac{\mathrm{d}r}{\mathrm{d}s} &= \cos\beta, \\ \frac{\mathrm{d}z}{\mathrm{d}s} &= \sin\beta, \\ \frac{\mathrm{d}\beta}{\mathrm{d}s} &= -Bo \times z - \frac{\sin\beta}{r} + \mu, \\ \frac{\mathrm{d}V}{\mathrm{d}s} &= \pi r^2 \sin\beta, \end{aligned}\right\} \tag{2.1a–d}$$

where $(r(s), z(s))$ is a parametrization of the interface generatrix by its arc length s, β is the inclination angle measured counterclockwise, $Bo \equiv \rho g {l_*}^2/\sigma$ is the Bond number with gravity g, surface tension σ and the characteristic length l_*, μ is a Lagrange multiplier, and V is the dimensionless volume. Note that (2.1*d*) is not necessary for defining the equilibrium, which is included to determine the drop volume (Del Río & Neumann 1997). In the following, unless otherwise stated, the dimensionless drop volume is always set to $2\pi/3$ (equal to the volume of a hemispherical drop of radius 1) to exclude the effect of drop volume. This helps us to focus on the effects of gravity. Thus the characteristic length is defined as $l_* = l_v \equiv (3v/2\pi)^{1/3}$ based on the actual drop volume v. Accordingly, the Bond number is given as

$$Bo = \frac{\rho g}{\sigma}\left(\frac{3v}{2\pi}\right)^{2/3}. \tag{2.2}$$

The system of (2.1) generally has no closed-form solutions, and must be integrated numerically together with the initial conditions

$$r(0) = z(0) = \beta(0) = V(0) = 0. \tag{2.3}$$

To begin integration, the relation $\sin\beta/r = \mu/2$ is used to remove the singularity of (2.1*c*) at $r = 0$ (Del Río & Neumann 1997). For given Bo and μ, we can determine uniquely a

solution curve $(r(s), z(s))$ and then obtain a drop shape by using the volume condition

$$V(s_c) = 2\pi/3, \tag{2.4}$$

where s_c denotes the arc length at the CL. However, we usually use the geometric condition (instead of unknown *a priori* μ)

$$\beta(s_c) = \alpha \quad \text{or} \quad r(s_c) = R \tag{2.5a,b}$$

to determine a drop with given Bo. The boundary value problem (2.1) with (2.3)–(2.5) for the equilibrium shape of pendant drops can be solved by the shooting method (see e.g. Del Rıo & Neumann 1997).

There may exist multiple equilibrium shapes for given parameters Bo and α (or R), some of which are stable, while others are unstable and cannot exist stably (Pozrikidis 2012). For given Bo and α, there may be two distinct stable pendant drops with pinned CLs (Pozrikidis 2012), which will be discussed in § 2.2.1. This suggests that (α, Bo) cannot be used as control parameters for uniquely determining the base state with a pinned CL. This issue will be addressed in the next section.

2.2. *Static stability*

2.2.1. *Axisymmetric perturbations*

The static stability of pendant drops can be examined by solving a series of intractable eigenvalue problems (Myshkis *et al.* 1987, pp. 129–130). For axisymmetric perturbations, an alternative is the PM method (Maddocks 1987) that determines stability from a family of equilibria. This method only requires solving the equilibrium problem (2.1) with (2.3)–(2.5) to obtain the diagram of volume $\tilde{V}$ against pressure $\tilde{P}$. The PM theory indicates the occurrence of instability along the counterclockwise direction through a TP (Lowry & Steen 1995). To draw the curve of $\tilde{V}$ versus $\tilde{P}$, here all drops are scaled by the capillary length $l_c = \sqrt{\sigma/\rho g}$ so that the volume is no longer fixed at $2\pi/3$. Due to the different scalings used here and in § 2.1, the relations between dimensionless parameters are given as follows:

$$\tilde{V} = \frac{2\pi}{3} Bo^{3/2}, \quad \tilde{P} = \frac{P}{\sqrt{Bo}}, \quad \tilde{\alpha} = \alpha, \quad \tilde{R} = \sqrt{Bo}\, R, \tag{2.6a–d}$$

where quantities with and without tildes correspond to the characteristic lengths of l_c and l_v, respectively. Tildes of α are omitted hereafter for simplicity.

Using the capillary length l_c as the characteristic length, the Young–Laplace equation (2.1) will change to a different dimensionless form (e.g. Sumesh & Govindarajan 2010; Zhang & Zhou 2020):

$$\frac{\mathrm{d}\tilde{r}}{\mathrm{d}\tilde{s}} = \cos\tilde{\beta}, \quad \frac{\mathrm{d}\tilde{z}}{\mathrm{d}\tilde{s}} = \sin\tilde{\beta}, \quad \frac{\mathrm{d}\tilde{\beta}}{\mathrm{d}\tilde{s}} = -\tilde{z} - \frac{\sin\tilde{\beta}}{\tilde{r}} + \tilde{\mu}, \quad \frac{\mathrm{d}\tilde{V}}{\mathrm{d}\tilde{s}} = \pi\tilde{r}^2 \sin\tilde{\beta}, \tag{2.7a–d}$$

where variables with tildes are dimensionless counterparts of variables in (2.1). With a variable $\tilde{\mu}$, (2.7) has a family of solutions (see the grey lines in figures 4*a*,*d*) for the initial conditions $\tilde{r}(0) = \tilde{z}(0) = \tilde{\beta}(0) = \tilde{V}(0) = 0$. In this case, one can easily impose a fixed contact angle condition $\tilde{\beta}(\tilde{s}_c) = \alpha$ (free CL) or a fixed CL boundary condition $\tilde{r}(\tilde{s}_c) = \tilde{R}$ (pinned CL).

Figures 4(*a*) and 4(*d*) show the curves of CL points for the boundary conditions $\alpha = 70^\circ$ and $\tilde{R} = 1$, respectively. Each point on the CL curves determines a pendant drop with

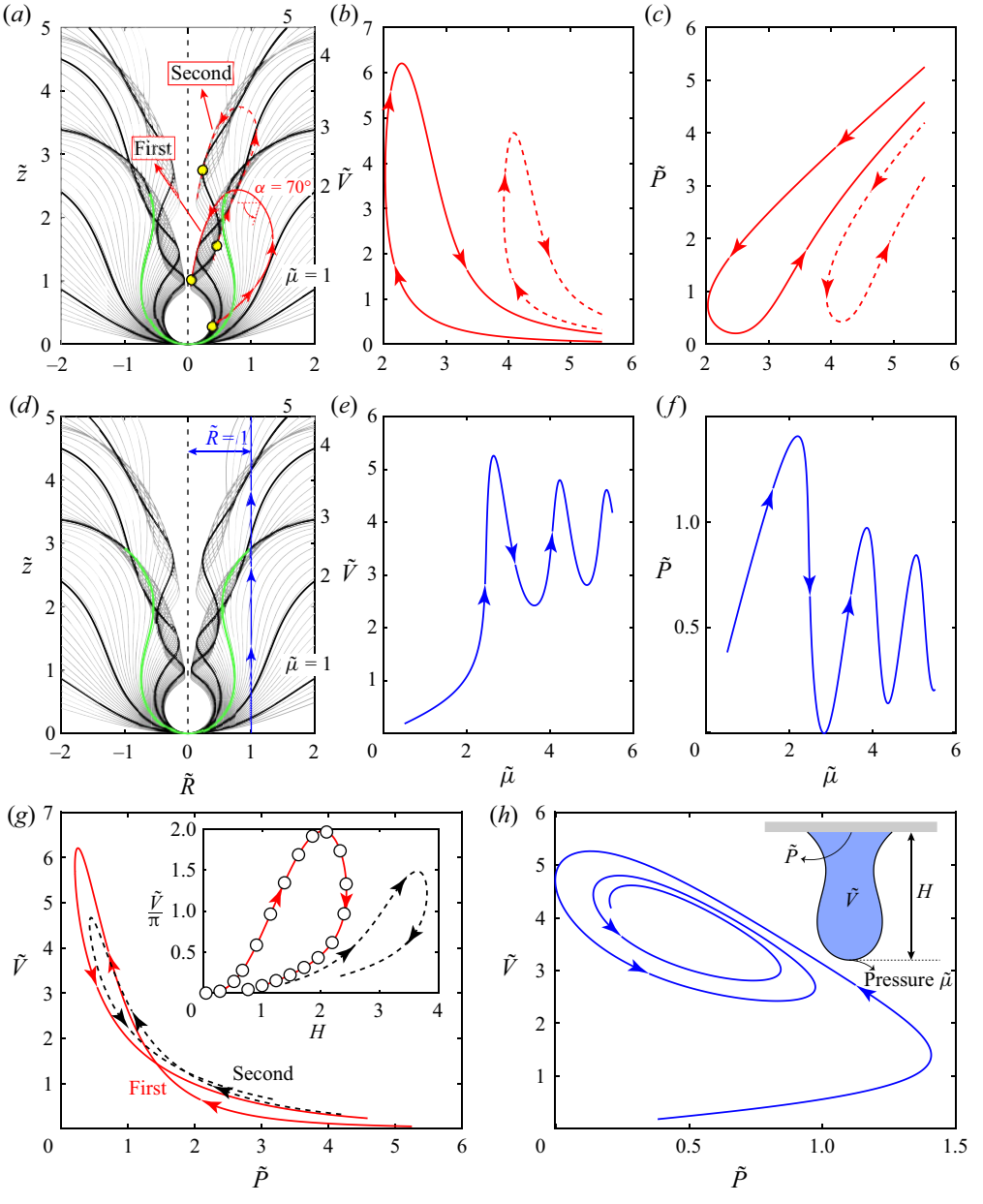

Figure 4. (*a*,*d*) The family of solution curves (grey lines) for the Young–Laplace equation (2.7), where five typical solution curves (black solid lines) are plotted for $\tilde{\mu} = 1, 2, 3, 4, 5$. The red and blue lines denote the boundary conditions (*a*) $\alpha = 70^\circ$ and (*d*) $\tilde{R} = 1$, respectively, where the arrows indicate the direction of instability. (*b*,*c*,*e*–*h*) The curves of volume $\tilde{V}$ versus $\tilde{\mu}$, pressure $\tilde{P}$ versus $\tilde{\mu}$, and $\tilde{V}$ versus $\tilde{P}$ for (*b*,*c*,*g*) $\alpha = 70^\circ$ and (*e*,*f*,*h*) $\tilde{R} = 1$. For $\alpha = 70^\circ$, the solid and dashed lines correspond to the first and second curves of CL points (yellow dots), respectively. The inset in (*g*) compares our results (red line) with those of Sumesh & Govindarajan (2010) (◯) for $\tilde{V}/\pi$ versus H with $\alpha = 70^\circ$. The inset in (*h*) shows a pendant drop scaled by l_c, where H is the drop height.

a given α or $\tilde{R}$, whose shape is the portion of the corresponding solution curve with a specific $\tilde{\mu}$ (see the green lines). For $\alpha = 70^\circ$, there can be multiple CL points (see the yellow dots) for one solution curve (e.g. with $\tilde{\mu} = 5$). The first and second CL points belong to the first CL curve, while the third and fourth points belong to the second CL curve. Accordingly, we can plot the curves of volume $\tilde{V}$ versus $\tilde{\mu}$, and pressure $\tilde{P}$ versus $\tilde{\mu}$, as shown in figures 4(*b*,*c*,*e*,*f*). Additionally, we compare our results with those of Sumesh & Govindarajan (2010) for $\tilde{V}/\pi$ versus drop height H, and find excellent agreement, as shown in the inset of figure 4(*g*). Here, the pressure $\tilde{P}$ is the pressure of the liquid on the wall, and $\tilde{\mu}$ is the pressure at the drop apex (see the inset of figure 4*h*), so the pressure $\tilde{P}$ required by the PM theory is given by $\tilde{P} = \tilde{\mu} - H$. From figures 4(*b*,*e*), we can see that there are multiple equilibria for certain volumes $\tilde{V}$, consistent with the results of Sumesh & Govindarajan (2010). Although we are only concerned with stable equilibrium, however, there may be two stable equilibria for pinned drops (Pozrikidis 2012). Multiple stable equilibria render it difficult to choose the control parameters to determine the pendant drop uniquely. Fortunately, by choosing the appropriate parameter space, only one of these equilibria is stable, which is related to the PM theory (Maddocks 1987).

Finally, the curves of $\tilde{V}$–$\tilde{P}$ can be drawn (see figures 4(*g*,*h*) for $\alpha = 70^\circ$ and $\tilde{R} = 1$). For fixed contact angle, the drops corresponding to the second $\tilde{V}$–$\tilde{P}$ curve (see figure 4*g*) are always unstable to both volume and pressure disturbances due to their multiple inflection points ($\mathrm{d}\beta/\mathrm{d}s = 0$) (Wente 1980; Sumesh & Govindarajan 2010). For simplicity in discussing stability, parts of the $\tilde{V}$–$\tilde{P}$ curves in figures 4(*g*,*h*) are reproduced in figure 5. Figure 5(*a*) shows the $\tilde{V}$–$\tilde{P}$ curves for drops with free CLs and $\alpha = 70^\circ$, where the horizontal and vertical TPs correspond to the stability changes to volume and pressure disturbances, respectively. Therefore, for volume disturbances, the equilibria are v-stable on the right-hand side of the horizontal TP, and v-unstable on the left-hand side, as indicated by the PM theory. For pressure disturbances, all pendant drops with free CLs are p-unstable in the same way as gravity-free drops, while pendant drops can be p-stable due to the stabilisation of CL pinning. Figure 5(*b*) shows the results for pinned CLs and $\tilde{R} = 1$. Pressure instability occurs at the first vertical TP (the right-hand one), and then there is a volume stability change through the horizontal TP. We recall that the gravity-free drops are always v-stable due to the absence of a horizontal TP (see figure 2). In contrast, pendant drops can be v-unstable under the destabilising effect of gravity. The stabilisation of CL pinning delays the onset of volume instability. For example, the drop $\tilde{A}$ with a free CL is v-unstable, while the drop $\tilde{D}$ with a pinned CL (having the same shape as the drop $\tilde{A}$) is v-stable.

Pozrikidis (2012) has demonstrated that there may exist two distinct v-stable drops with pinned CLs for given α and $\tilde{V}$ (e.g. pinned drops with the same shape as $\tilde{A}$ and $\tilde{B}$, denoted by $\tilde{A}_p$ and $\tilde{B}_p$, respectively). Note that though the drop $\tilde{A}$ is v-unstable, the drop $\tilde{A}_p$ with pinned CL (i.e. $\tilde{D}$) is v-stable due to the stabilisation of CL pinning (see figure 5*b*). Therefore, the distinct drops $\tilde{A}_p$ and $\tilde{B}_p$ are both v-stable and have the same contact angle α and volume $\tilde{V}$ (or Bo). This implies that the parameter pair (α, Bo) cannot define uniquely the base state with a pinned CL. Knowing that only one branch of solutions in the fold bifurcation is stable (Maddocks 1987), this indicates that the parameter pair (R, Bo) can determine uniquely a stable drop with pinned CL. Thus in the following, the base states (stable) with free and pinned CLs for dynamic stability are governed by the control parameters (α, Bo) and (R, Bo), respectively.

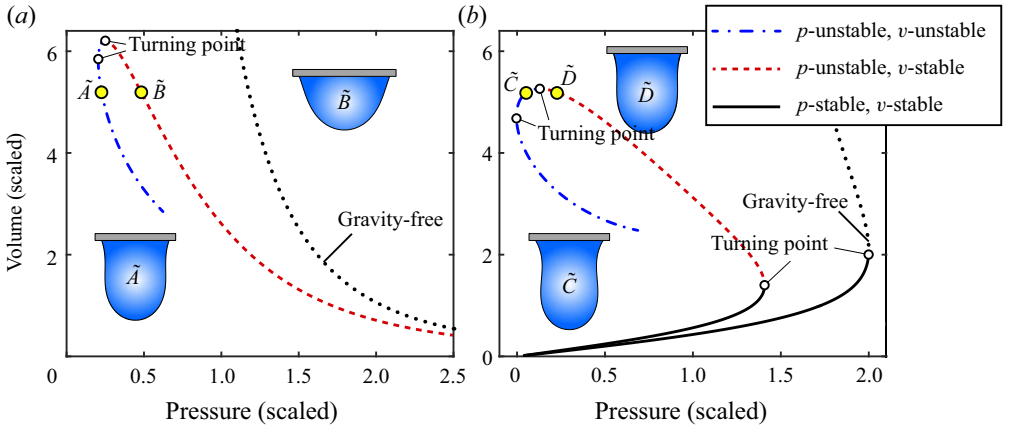

Figure 5. Volume–pressure ($\tilde{V}$–$\tilde{P}$) diagrams of pendant drops with (*a*) free CLs and $\alpha = 70°$, and (*b*) pinned CLs and $\tilde{R} = 1$. Instability occurs at the TPs (hollow circles) along the counterclockwise direction. In (*a*), drops $\tilde{A}$ and $\tilde{B}$ are v-unstable and v-stable, respectively, but both are p-unstable. In (*b*), the drop $\tilde{D}$ with the same shape as $\tilde{A}$ (v-unstable), however, is v-stable due to the stabilising effect of the pinned CL. All gravity-free drops are v-stable. Here, the characteristic length l_* is the capillary length $l_c = \sqrt{\sigma/\rho g}$.

To summarize briefly, the PM theory states that the pendant drop is v-stable (p-stable) to axisymmetric perturbations before its volume (pressure) reaches a maximum. In contrast to sessile drops, pendant drops can be v-unstable destabilised by gravity. Note that static stability is maintained for different scalings, thus these conclusions hold for drops with fixed volume in § 2.1.

2.2.2. *Non-axisymmetric perturbations*

The PM method described above deals with only static stability for axisymmetric perturbations (Bostwick & Steen 2015). Fortunately, for non-axisymmetric perturbations, the static stability of a pendant drop can be determined by comparing the boundary parameter χ with the critical boundary value $\chi^*_{1,1}$ (Myshkis *et al.* 1987; Zhang & Zhou 2020), referred to as the boundary parameter comparison approach. The critical boundary value $\chi^*_{1,1}$ corresponds to the $\{1, 1\}$ mode, which is the most dangerous among non-axisymmetric perturbations, given by (see Myshkis *et al.* 1987, p. 141)

$$\chi^*_{1,1} = -\frac{r'(s_c)}{z'(s_c)} K_1(s_c) = -K_1(s_c)\cot\alpha, \tag{2.8}$$

where the prime denotes the derivative with respect to arc length s, s_c is the arc length at the CL, and $K_1 = \mathrm{d}\beta/\mathrm{d}s$ is the signed curvature of the drop profile. The boundary parameter χ measures the degree of CL pinning, expressed in terms of the included angle $\pi - \alpha$ between $\boldsymbol{n}$ and $\boldsymbol{n}_s$ (figure 3*a*), and the liquid K_1 and solid $\bar{K}$ curvatures at the CL, as

$$\chi = \frac{K_1(s_c)\cos(\pi - \alpha) - \bar{K}}{\sin(\pi - \alpha)}, \tag{2.9}$$

where the curvature of the solid surface is $\bar{K} < 0$ if the solid is convex to the liquid, $\bar{K} = 0$ for a flat solid surface, and $\bar{K} > 0$ otherwise (Myshkis *et al.* 1987).

We determine the stability as follows: the drop is stable if $\chi > \chi^*_{1,1}$, is marginally stable (i.e. with a zero eigenvalue) when $\chi = \chi^*_{1,1}$, and otherwise unstable. Note that

all non-axisymmetric perturbations automatically satisfy volume conservation, so volume and pressure disturbances are not distinguishable in this case. We have the solid curvature $\bar{K} = 0$ for free CLs and $\bar{K} = -\infty$ for pinned CLs, since the pinned CL can be regarded as a CL at a convex edge with an infinitesimal curvature radius (Myshkis *et al.* 1987). Comparing (2.9) and (2.8) yields

$$\chi = \chi^*_{1,1} = -K_1(s_c)\cot\alpha \tag{2.10}$$

for free CLs, and

$$\chi = +\infty > \chi^*_{1,1} \tag{2.11}$$

for pinned CLs. Thus for non-axisymmetric perturbations, pendant drops with pinned CLs are stable, while drops with free CLs are marginally stable, leading to a zero frequency mode $\{1, 1\}$ (see § 3.4). This is consistent with the physical intuition that drops with free CLs on a plane have horizontal translational invariance (Zhang *et al.* 2023).

2.3. *Dynamic stability*

2.3.1. *Eigenvalue problems for natural oscillations*

We restrict ourselves to the dynamic stability of stable drops with a volume constraint. In this case, stable drops exhibit natural oscillations, which reflect their dynamic stability. To study natural oscillations of pendant drops (figure 3*a*), we need to solve the following functional eigenvalue problem (Myshkis *et al.* 1987; Zhang *et al.* 2023):

$$\frac{1}{r}\frac{\partial}{\partial r}\left(r\frac{\partial\phi}{\partial r}\right) + \frac{\partial^2\phi}{\partial z^2} - \frac{l^2}{r^2}\phi = 0 \quad [D], \tag{2.12a}$$

$$\frac{\partial\phi}{\partial n} = 0 \quad [\partial D^s], \tag{2.12b}$$

$$\left(\frac{\partial\phi}{\partial n}\right)'' + \frac{r'}{r}\left(\frac{\partial\phi}{\partial n}\right)' + \left[Bo\times r' + \left({K_1}^2 + {K_2}^2\right) - \frac{l^2}{r^2}\right]\frac{\partial\phi}{\partial n} = -\lambda^2\phi \quad [\partial D^f], \tag{2.12c}$$

$$\int_\Gamma \frac{\partial\phi}{\partial n}\,\mathrm{d}\Gamma = 0 \quad [\partial D^f], \tag{2.12d}$$

$$\left(\frac{\partial\phi}{\partial n}\right)' + \chi\frac{\partial\phi}{\partial n} = 0\Big|_{s=s_c} \quad [\gamma], \tag{2.12e}$$

where ϕ and $\partial\phi/\partial n$ are the potential function and its normal derivative, respectively, λ is the dimensionless frequency (scaled by the characteristic time $t_* = \sqrt{\rho l_*^3/\sigma}$ with $l_* = l_v$), and $K_1 = \mathrm{d}\beta/\mathrm{d}s$ and $K_2 = \sin\beta/r$ are the two principle curvatures of the drop surface.

Substituting (2.10) and (2.11) into (2.12*e*), we obtain the free CL condition

$$\left(\frac{\partial\phi}{\partial n}\right)' - K_1\cot\alpha\frac{\partial\phi}{\partial n} = 0\Big|_{s=s_c}, \tag{2.13}$$

and the pinned CL condition

$$\frac{\partial\phi}{\partial n} = 0\Big|_{s=s_c}, \tag{2.14}$$

respectively.

The eigenvalue problem (2.12) is derived from potential flow theory and linearised governing equations on the boundary via the normal mode decomposition and separation of variables method (see e.g. Bostwick & Steen 2014; Zhang *et al.* 2023). Equation (2.12*a*) is Laplace's equation written in cylindrical coordinates (r, z), (2.12*b*) is the no-penetration condition on the solid surface, (2.12*d*) is the condition of volume conservation, (2.12*c*) is the free-surface governing equation derived from the kinematic condition and the dynamic pressure balance, and (2.12*e*) is the CL condition. The solutions of the eigenvalue problem (2.12) give the dimensionless frequencies λ and mode shapes $\partial\phi/\partial n$. Since the frequency squared λ^2 is inversely proportional to the drop volume (Noblin *et al.* 2004), we adopt a characteristic length $l_v = (3v/2\pi)^{1/3}$, fixing the drop volume at $2\pi/3$ to exclude the volume effect. Therefore, the real frequency $f \equiv \lambda/(2\pi t_*)$ (in Hz) is given as

$$f^2 = \left(\frac{\rho}{\sigma}\right)^{1/2}\left(\frac{g}{Bo}\right)^{3/2}\left(\frac{\lambda}{2\pi}\right)^2 = \frac{\sigma}{6\pi\rho v}\lambda^2. \tag{2.15}$$

2.3.2. *Boundary element model and mode classification*

Theoretical methods (e.g. Lyubimov *et al.* 2006; Bostwick & Steen 2014; Sharma & Wilson 2021) for solving the eigenvalue problem (2.12) usually require drops to be hemispheres or spherical caps. The BE model developed in Zhang *et al.* (2023) can deal with drops of arbitrary shape and has been applied successfully to gravity-flattened sessile drops, so it is also applicable to our problem. We adopt the BE model to solve numerically the eigenvalue problem (2.12). The fundamental procedures for constructing the BE model can be found in Appendix A. One can refer to Zhang *et al.* (2023) for more details on the formulation of the BE model.

The solutions of the BE model give the natural frequencies and mode shapes. Analogous to spherical harmonics, these modes can be categorised into zonal $[k, l = 0]$, sectoral $[k, l = k > 0]$ and tesseral $[k > l, l > 0]$ modes according to polar k and azimuthal l wavenumbers (Bostwick & Steen 2014). In experiments (Chang *et al.* 2013, 2015), another more intuitive layer–sector classification $\{n, l\}$ is usually used for identifying the number $n = (k - l)/2 + 1$ of vertical layers, so that zonal, sectoral and tesseral modes are labelled as $\{n \geqslant 2, l = 0\}$, $\{n = 1, l > 0\}$ and $\{n > 1, l > 0\}$, respectively. In terms of mode shape, the zonal mode is axisymmetric, the sectoral mode is star-shaped, and the tesseral mode has a complex wave pattern, as shown in figure 6. One of the rocking $l = 1$ modes with one sector rocking from side to side is also drawn, and the rocking modes are particularly easy to identify in experiments. Besides, the directional movement of drops on a vibrating plate is attributed to the rocking modes (Ding *et al.* 2018; Costalonga & Brunet 2020).

3. Numerical results and discussion

3.1. *Verification*

The BE model has been well validated for gravity-free drops and gravity-flattened sessile drops in Zhang *et al.* (2023). The natural frequencies of pendant drops are verified here. Figure 7 compares the experimental results of DePaoli, Scott & Basaran (1992) with the inviscid results of the BE model for zonal mode $\{2, 0\}$ with pinned CL. It is shown that for CL diameter $D = 0.16$ cm, the BE results of small drops are overpredicted, while the results of large drops agree well. This is due to the great viscous effect of small drops, which significantly reduces the resonant frequency (Lyubimov *et al.* 2006; Chang *et al.* 2015), while the viscous effect is negligible for large drops with low Ohnesorge numbers. However, for the CL 0.068 cm, our predictions are underestimated for large drops.

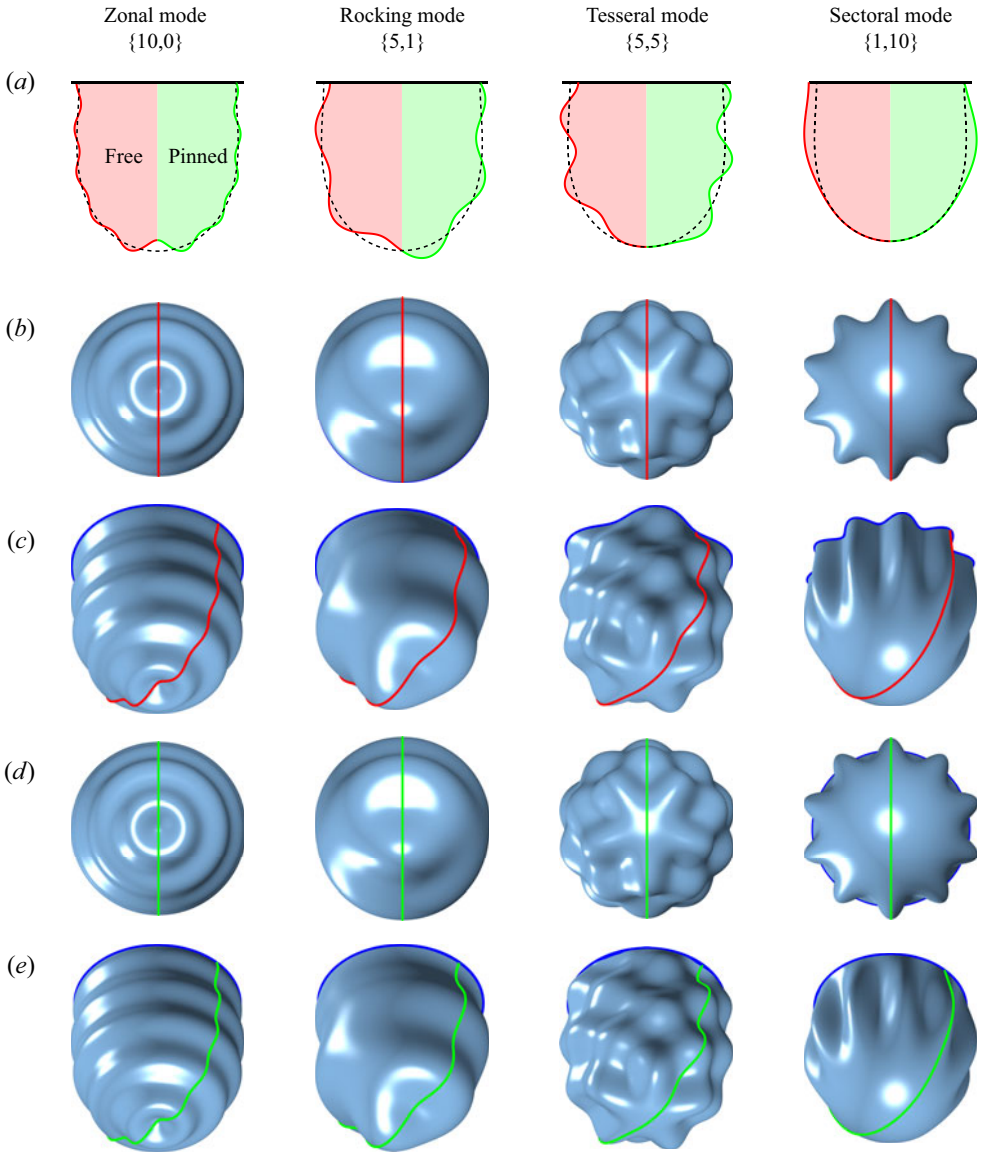

Figure 6. Typical mode shapes for a pendant drop with $Bo = 1.4$, $\alpha = 90^\circ$ and $R = 0.7$ in (a) cross-sectional and three-dimensional (c,e) oblique and (b,d) bottom views. The modes with free and pinned CLs are indicated by the red and green lines, respectively.

A reasonable explanation is that the drop volume might be measured inaccurately in the experiment, because volume values of large drops in experimental data exceed the volume of the maximum drop (yellow dot), indicating that these drops cannot exist stably.

Interestingly, our results show that there is a sharp fall in frequency to zero near the maximum drop point. This suggests that the frequency of pendant drops near the maximum drop point is highly sensitive to the drop volume. Furthermore, the numerical results show that the zonal mode $\{2, 0\}$ of the maximum drop has zero frequency. This is consistent with the maximum drop being marginally stable indicated by the PM theory (see the inset in figure 7), further validating the accuracy of the BE model.

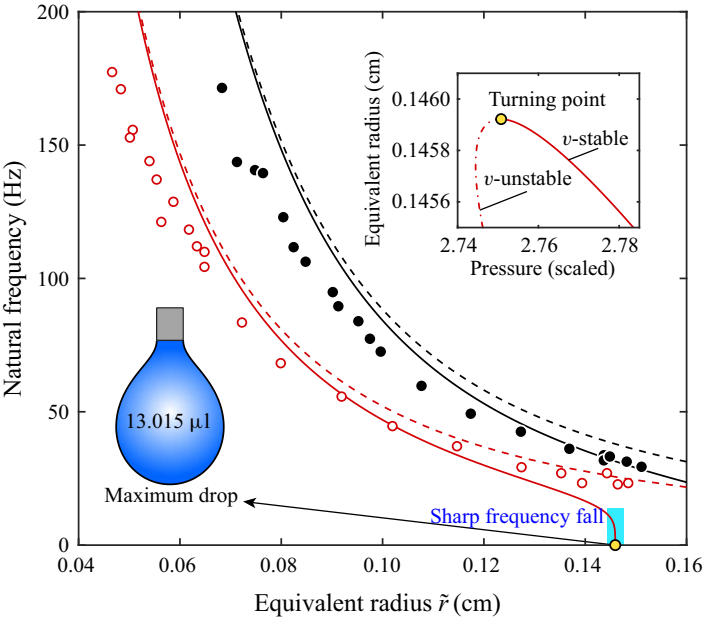

Figure 7. Frequency of zonal mode $\{2, 0\}$ with pinned CL against equivalent radius $\tilde{r} = (3v/4\pi)^{1/3}$. The numerical results of the BE model (solid lines) are compared with the experimental results of DePaoli *et al.* (1992) (dots) for CL diameters $D = 0.068$ cm (red) and 0.16 cm (black). The BE results without gravity (dashed lines) are drawn for comparison. For $D = 0.068$ cm, the maximum drop (yellow dot) corresponds to the horizontal TP (the right-hand inset; see also figure 5). The physical parameters used here are $\rho = 997$ kg m^{-3}, $\sigma = 0.072$ N m^{-1} and $g = 9.81$ m s^{-2}. A sharp fall in frequency is highlighted by the cyan region.

3.2. *Stability limits: maximum Bo*

As shown above, the maximum drop (with the maximum Bond number Bo_{max}) determines the stability limit. Figures 8(*a*,*b*) plot the maximum Bond number Bo_{max} against contact angle α and CL radius R, respectively, for free and pinned CLs. Results show that for free CLs, Bo_{max} decreases with increasing α, consistent with the physical intuition that more hydrophilic surfaces can suspend larger drops. For pinned CLs, however, Bo_{max} increases and then decreases with increasing R (figure 8*b*). At $R = R^* = 1.5445$, Bo_{max} reaches its maximum, and the corresponding drop (labelled G) has a zero contact angle, which has the same shape as the maximum drop A (with $\alpha = 0°$) for free CLs. This is due to the indistinguishability of the free and pinned CLs for $\alpha = 0°$, both having the boundary parameter $\chi = +\infty$. For $R > R^*$, the marginally v-stable drops with $\alpha < 0°$ are non-physical (see the drop $\bar{H}$) so that Bo_{max} corresponds to v-stable drops with $\alpha = 0°$ (e.g. H). Thus the static stability limits are determined by the maximum Bond numbers Bo_{max} corresponding to marginally v-stable drops, except for $R > R^*$. The curves of Bo_{max} versus α, and Bo_{max} versus R, divide the parameter spaces into regions where equilibrium exists and regions where it does not, labelled as equilibrium and non-equilibrium, respectively. In the equilibrium region, multiple equilibria exist and the only v-stable equilibrium can be determined through the PM theory, as shown in figures 8(*c–f*). We are concerned only with the dynamic stability of v-stable equilibria in the following.

Figure 9(*a*) plots the frequency $\lambda_{2,0}$ of zonal mode $\{2, 0\}$ against Bo for free CLs with four different contact angles. For contact angles $\alpha = 50°$, $100°$ and $150°$, the frequencies

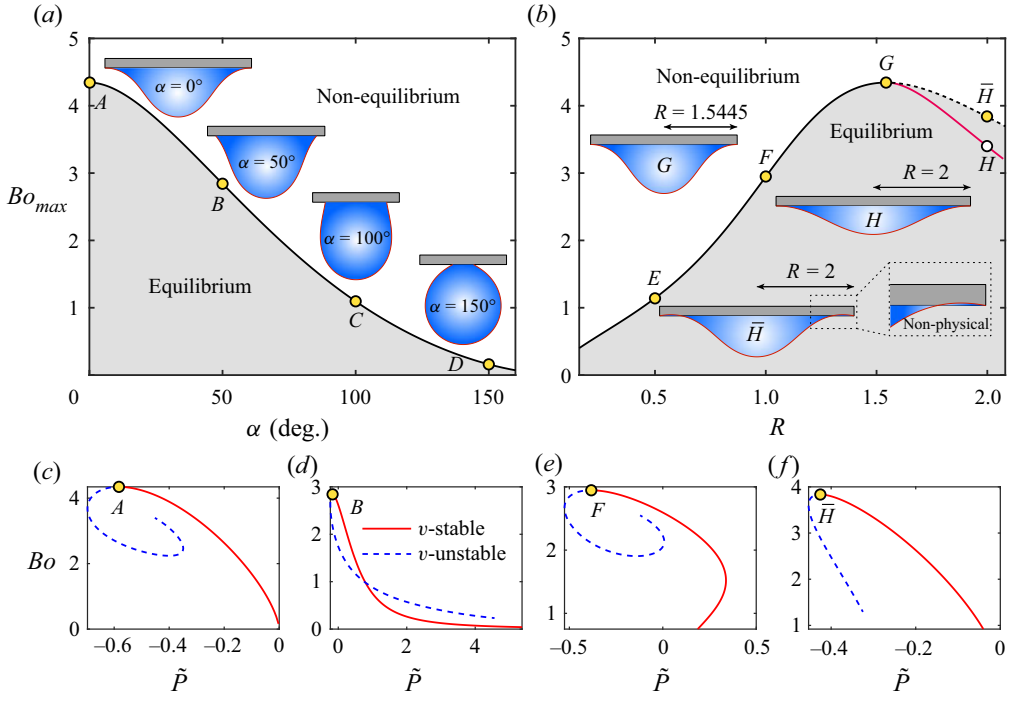

Figure 8. (*a*,*b*) Maximum Bond number Bo_{max} versus (*a*) contact angle α for free CLs, and (*b*) CL radius R for pinned CLs. The black solid and black dashed lines correspond to marginally v-stable drops with $\alpha \geqslant 0^\circ$ and $\alpha < 0^\circ$, respectively. In (*b*), the red solid line corresponds to drops with $\alpha = 0^\circ$. (*c*–*f*) The curves of Bo versus $\tilde{P}$ for (*c*) drop A with $\alpha = 0^\circ$, (*d*) drop B with $\alpha = 50^\circ$, (*e*) drop F with $R = 1$, and (*f*) drop $\bar{H}$ with $R = 2$. The maximum Bond numbers Bo_{max} correspond to the horizontal TPs of the $\tilde{P}$–$\tilde{V}$ curves due to $Bo = (3\tilde{V}/2\pi)^{2/3}$ (see (2.6*a*–*d*)).

decrease with increasing Bo, consistent with the numerical results of DePaoli *et al.* (1992). However, for a very small contact angle $\alpha = 0^\circ$, the frequency initially increases and then decreases. The initial increase of frequency seems counterintuitive, because gravity reduces the restoring force and makes the pendant drop slender, both of which decrease frequency in most cases (Basaran 1992; Ibrahim 2005; Temperton *et al.* 2015). This suggests that the deformation of pendant drops with small α increases the frequency at low gravity. For pinned CLs, the frequencies always decrease with increasing Bo regardless of the CL radius R, as shown in figure 9(*b*). We also observe zero frequency modes $\{2, 0\}$ at Bo_{max}, except for the non-marginally stable drop H. Note that although the numerical results of $\lambda_{2,0}$ cannot be exactly zero, one can verify our results converging to zero by grid refinement, as will be discussed in § 3.4. Therefore, the static stability of pendant drops can be recovered by letting $\lambda_{2,0} = 0$ in the dynamic stability, and the critical conditions for static and dynamic stability are essentially the same.

Furthermore, we observe sharp frequency falls when approaching Bo_{max}, except for the drop H. The sharp fall in $\lambda_{2,0}$ may be explained by the fact that the base state near Bo_{max} (see the horizontal TP in figure 5) is sensitive to volume or gravity (i.e. a small change in volume leads to a large change in pressure). When approaching Bo_{max}, other modes are also sensitive to Bo, leading to similar sharp changes in frequency (see figure 13). We note that the sharp change in frequency with respect to wavenumber k is also observed for the rotating Rayleigh–Plateau instability near stability thresholds (Dubey, Roy & Subramanian 2022). The sharp frequency changes may lead to inaccurate theoretical

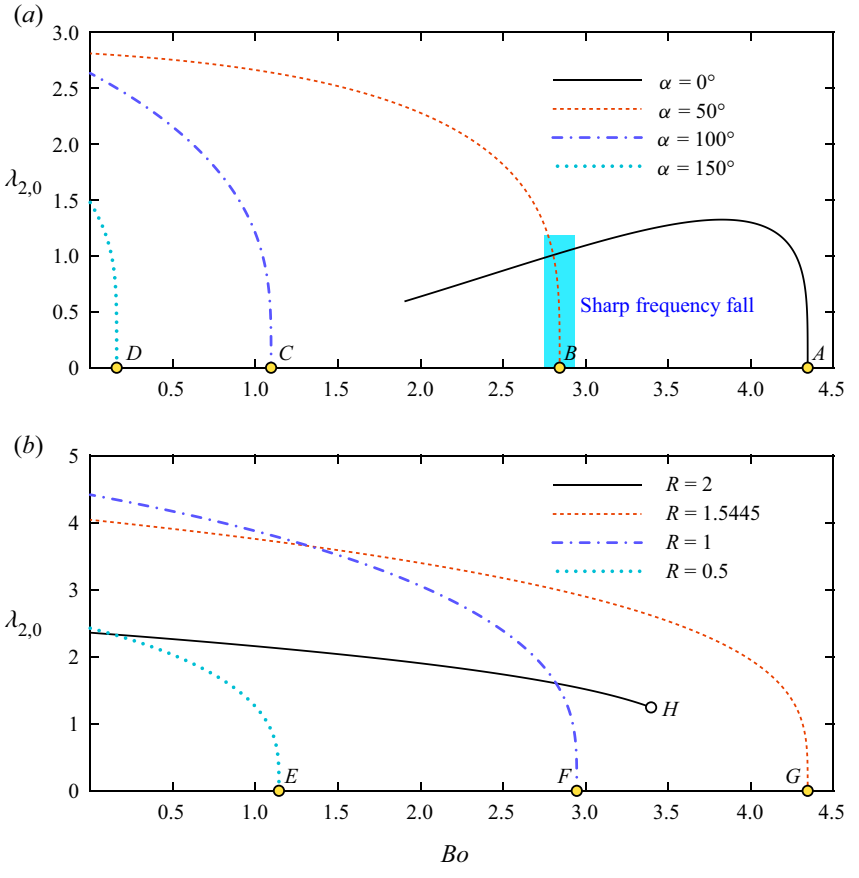

Figure 9. Frequency of zonal mode $\{2, 0\}$ against the Bond number Bo for (a) free and (b) pinned CLs. The eight points A–H correspond to the maximum Bond number Bo_{max} (i.e. drops A–H in figure 8). The cyan region highlights a sharp fall in frequency.

predictions near Bo_{max}, affecting relevant applications such as surface tension measurements via oscillation (Mollot *et al.* 1993; Chang & Franses 1994). Therefore, for better predictions, experiments on pendant drops that are close to marginally v-stable should be avoided.

3.3. *Frequency shifts due to gravity*

To measure how gravity affects the frequency spectrum, we define the shift factor $S_{n,l}$ of frequency for each mode $\{n, l\}$ as follows:

$$S^f_{n,l}(\alpha, Bo) = \frac{\lambda^f_{n,l}(\alpha, Bo)}{\lambda^f_{n,l}(\alpha, 0)} - 1, \quad \text{free CLs}, \tag{3.1a}$$

$$S^p_{n,l}(R, Bo) = \frac{\lambda^p_{n,l}(R, Bo)}{\lambda^p_{n,l}(R, 0)} - 1, \quad \text{pinned CLs}. \tag{3.1b}$$

The value of $S_{n,l}$ denotes the relative change of frequency and $S_{n,l} > 0$ (<0) indicates an upward (downward) shift of frequency due to gravity. In (3.1), the control parameters are

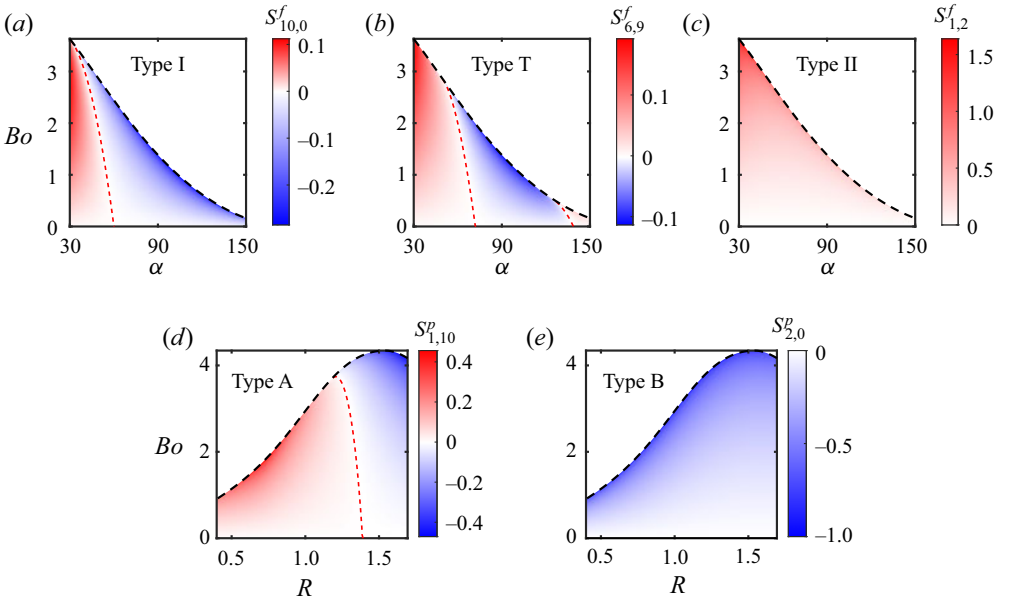

Figure 10. Five typical contour diagrams of shift factor $S_{n,l}$. (*a–c*) Types I, T and II correspond to modes $\{10, 0\}$, $\{6, 9\}$ and $\{1, 2\}$ with free CLs, respectively. (*d*,*e*) Types A and B correspond to modes $\{1, 10\}$ and $\{2, 0\}$ with pinned CLs, respectively. The black dashed and red dashed lines indicate Bo_{max} (see figure 8) and $S_{n,l} = 0$, respectively.

chosen as (α, Bo) and (R, Bo) for free and pinned CLs, respectively, to determine the base state uniquely (see § 2.2.1).

Figure 10 shows five typical phase diagrams of how gravity shifts the natural frequencies of pendant drops. For free CLs, there are three types (I, II and T) of contour diagrams of $S^f_{n,l}$, as shown in figures 10(*a–c*). For type I, there is a longitudinally inclined critical line $S^f_{n,l} = 0$, a region $S^f_{n,l} > 0$ (red) on the left-hand side of the critical line, and a region $S^f_{n,l} < 0$ (blue) on the right-hand side. This means that the frequency of the mode of type I with small (large) contact angles increases (decreases) under gravity. For type II, we observe $S^f_{n,l} > 0$ regardless of α and Bo, which implies that gravity always increases the frequency. The diagram of type T presents a complex pattern of gravity affecting frequency, which is a transition between types I and II. The three patterns are generally opposite to those of sessile drops (Zhang *et al.* 2023), as the direction of gravity is reversed for pendant drops and sessile drops. For pinned CLs, there are two types (A and B) of diagrams of $S^p_{n,l}$ (figures 10*d*,*e*). The diagram of type A indicates that gravity decreases (increases) the frequency for modes with small (large) CL radii R (figure 10*d*). For type B, gravity always decreases the frequency (figure 10*e*).

Figure 11 presents the classifications of the $S_{n,l}$ diagrams according to the mode numbers $\{n, l\}$. For free CLs, modes with larger n (l) are more likely to be type I (II), and the remaining modes in the middle are type T. As a consequence, all zonal modes are of type I, and most sectoral modes are of type II. For pinned CLs, the modes with $l > n$ ($l < n$) are of type A (B), and modes $\{n, l = n\}$ are possible for both. Therefore, all zonal and sectoral modes with pinned CLs are of type B and A, respectively. The above findings provide an overview of gravity affecting natural frequencies for pendant drops, and complement the study of the effects of gravity on partially wetting drops (Zhang *et al.* 2023).

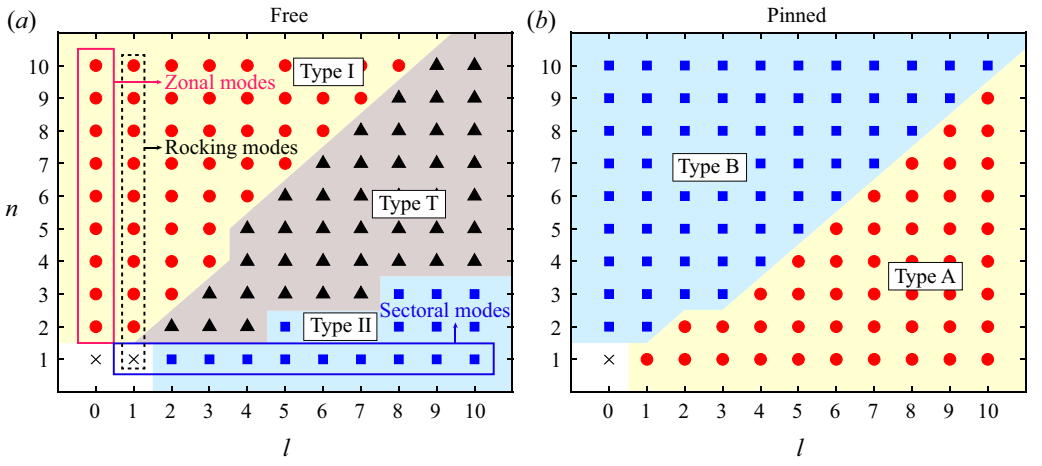

Figure 11. Types of contour diagrams of $S_{n,l}$ for modes with (*a*) free and (*b*) pinned CLs, where $n = 1, 2, \ldots, 10$ and $l = 0, 1, \ldots, 10$.

The above findings show that the frequency shifts due to gravity compared to the gravity-free case are complex, depending on the modal pair $\{n, l\}$, the Bond number Bo, and the contact angle α or CL radius R. Intuitively, gravity is supposed to decrease the frequency of pendant drops due to gravity acting as a destabilising force, in agreement with the experimental and numerical observations (DePaoli *et al.* 1992; Basaran & DePaoli 1994). However, gravity also distorts the base state (elongated) and thus affects the frequency indirectly. Since the vibrations of sessile/pendant drops might be analogous to liquid sloshing in an upright cylindrical container (Noblin, Buguin & Brochard-Wyart 2009; Temperton *et al.* 2015), the drop elongation can be characterised by an increase in mean height of the liquid in the cylinder, which increases the frequencies, while gravity as a destabilising force always decreases the frequencies (Temperton *et al.* 2015). Therefore, the competing effects of the reduced restoring force and base state elongation due to gravity lead to the above complex dependence of the frequencies on gravity.

3.4. *Zero frequency modes* {2, 0} *and* {1, 1}

Two modes of pendant drops can have zero frequency: the zonal {2, 0} and Noether {1, 1} modes. The results of $\lambda_{1,1} = 0$ for free CLs are not surprising, because the Noether mode {1, 1} reflects the horizontal displacement of the drop and has zero frequency according to Noether's theorem when its base state has the horizontal translational invariance. Bostwick & Steen (2014) noticed that the symmetry of translational invariance can be broken by CL pinning or changing the wetting parameter, resulting in a non-zero frequency of the Noether mode. However, varying contact angle or exerting gravity does not break this symmetry, so that gravity-flattened sessile drops with free CLs always have the zero frequency mode {1, 1} (Zhang *et al.* 2023).

Obviously, pendant drops with free CLs on a plane also have horizontal translational invariance, indicating that their Noether mode {1, 1} has zero frequency regardless of α and Bo. For verification purposes, figure 12 plots the BE results of $|\lambda_{1,1}^2|$ against the inverse $1/N$ of the grid number in log-log scale. Here, the grid number N is the number of BEs of the liquid surface (see figure 15). The power laws $|\lambda_{1,1}^2| \propto (1/N)^c$ with exponents $c \sim 2$ are found for two cases, ($\alpha = 50^\circ$, $Bo = 2$) and (100°, 1). The exponents $c \sim 2$ reflect the

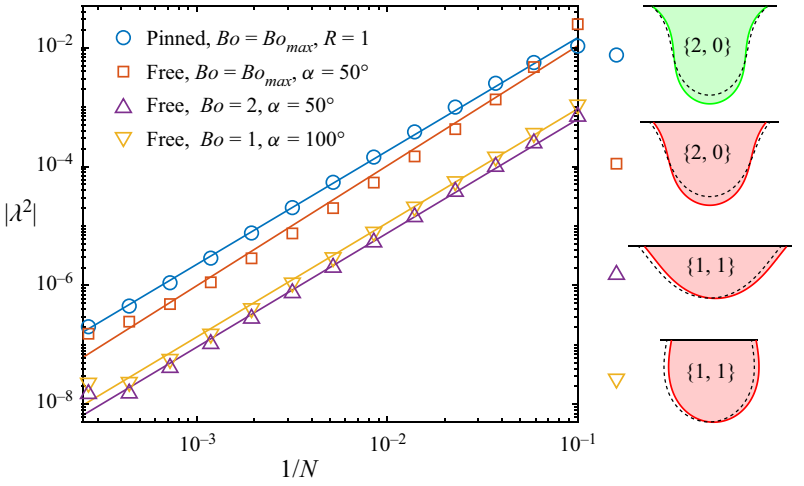

Figure 12. Numerical results of the absolute value $|\lambda^2|$ of frequency squared versus the grid number inverse $1/N$ of the BE model for zonal $\{2, 0\}$ (◯, □) and Noether $\{1, 1\}$ (△, ▽) modes. The frequencies decay to zero in power laws $|\lambda^2| \propto N^{-c}$ with exponents $c \sim 2$ for these modes, as indicated by the lines fitted by least squares.

second-order convergence of the BE model (Zhang *et al.* 2023). Therefore, one can expect that the numerical results of $\lambda_{1,1}$ decay to zero as the grid number N increases. The results of $\lambda_{1,1} = 0$ are also consistent with the prediction by the boundary parameter comparison approach (§ 2.2.2), which suggests that pendant drops with free CLs are marginally stable to non-axisymmetric perturbations.

A new feature of pendant drops is their zero frequency mode $\{2, 0\}$ at Bo_{max}. Figure 12 confirms $\lambda_{2,0} = 0$ of the maximum drops B and F (figure 8) by the power laws $|\lambda^2_{2,0}| \propto N^{-c}$ with $c \sim 2$. Due to the destabilisation of gravity, pendant drops can detach from the wall or pinch off under gravity (Henderson *et al.* 1997), reflecting the capillary instability related to the zonal mode $\{2, 0\}$. This instability occurs when the drop volume exceeds the maximum volume (i.e. Bo_{max}). As stated in § 3.2, the pendant drop with Bo_{max} corresponding to the horizontal TP is marginally v-stable (see figure 5) and has the zero frequency mode $\{2, 0\}$. This suggests that the static stability of pendant drops can be recovered by letting $\lambda_{2,0} = 0$ in the dynamic stability, and the critical conditions for static and dynamic stability are essentially the same.

Additionally, the zero frequency mode $\{2, 0\}$ with Bo_{max} can also be used to define the characteristic length scale of instability for pendant drops. For the Rayleigh–Plateau instability of a liquid cylinder of radius r_0, the critical wavelength $L_{RP} = 2\pi r_0$ (with dimensionless wavenumber $k = 1$) is usually used to define the characteristic length scale of critical instability (Plateau 1873). Similarly, the pendant drops also have critical states of instability corresponding to the $\{2, 0\}$ mode with $k = 2$. Thus a characteristic length scale can be defined as $L = 2\pi l_*/k = \pi l_*$ based on the wavelength of the $\{2, 0\}$ mode. The critical value of $l_* = \sqrt{\sigma Bo/\rho g}$ is reached at $Bo = Bo_{max}$. Therefore, for pendant drops, the characteristic length scale of critical instability is given as $L = \pi\sqrt{\sigma\, Bo_{max}/\rho g} = \pi\, Bo_{max}^{1/2}\, l_c$, where Bo_{max} depends on α or R (see figure 8). It can be seen that the characteristic length scale L is related to the capillary length l_c and the maximum Bond number Bo_{max}.

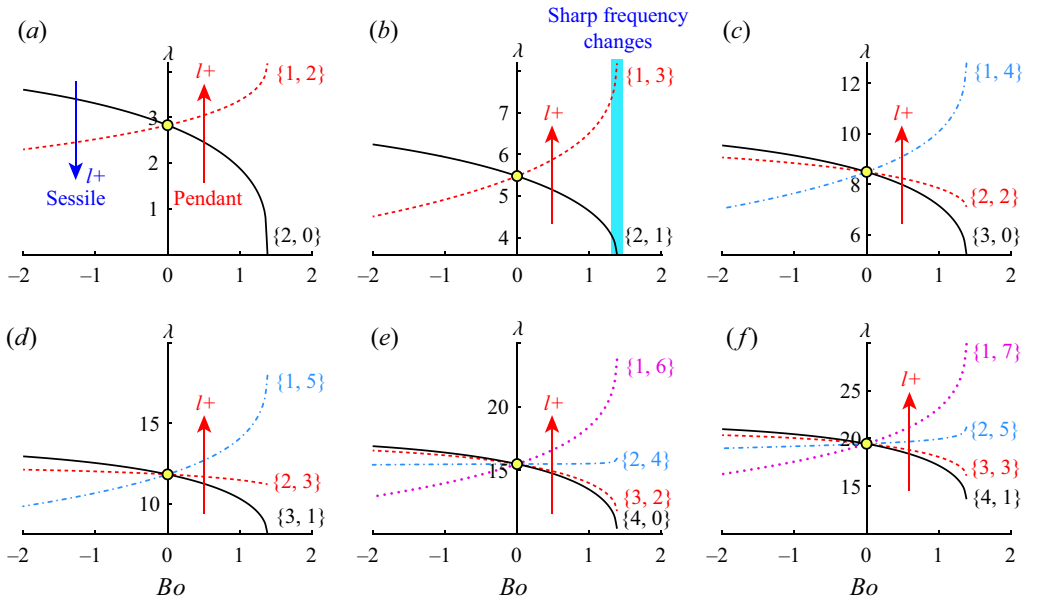

Figure 13. Breaking of the spectral degeneracy due to gravity: frequency $\lambda_{n,l}$ versus the Bond number Bo for (*a*) $k = 2$, (*b*) $k = 3$, (*c*) $k = 4$, (*d*) $k = 5$, (*e*) $k = 6$, and (*f*) $k = 7$, where the layer number is $n = (k - l + 2)/2$. The yellow dots indicate the spectral degeneracy of free semi-drops with $\lambda^2 = k(k-1)(k+2)$ (see also Bostwick & Steen 2014, figure 2). The cyan region highlights sharp frequency changes near Bo_{max}.

3.5. *Breaking of spectral degeneracy and spectral ordering*

For free semi-drops (with $\alpha = 90°$, $R = 1$, $Bo = 0$ and free CLs), CL pinning or varying contact angle breaks the spectral degeneracy inherited from the RL spectrum (Lyubimov *et al.* 2006; Bostwick & Steen 2014). Figure 13 shows that gravity breaks the spectral degeneracy, where the spectral splitting exhibits the larger (smaller) frequency for pendant (sessile) drops with the higher l (see the direction of the arrows). The spectral splitting due to gravity for $Bo > 0$ (pendant) is similar to those of varying contact angle for $\alpha > 90°$ and CL pinning (Lyubimov *et al.* 2006; Bostwick & Steen 2014). Specifically, there are two opposite kinds of spectral splitting: the higher the l, the larger the frequency for $Bo > 0$, CL pinning and $\alpha > 90°$, and the reverse holds for $Bo < 0$ and $\alpha < 90°$. The two kinds of spectral splitting arising from the breaking of spectral degeneracy are associated with the construction of periodic tables (PTs) of modes (Steen *et al.* 2019).

Steen *et al.* (2019) used an analogy of the PT of chemical elements to categorise the modes of spherical cap drops into two standard PTs and other non-standard PTs with irregularities, where modes are ordered according to the kinetic energy (or frequency). In the two standard PTs, the modes are first sorted in ascending order of k, and then modes with the same k are sorted in descending or ascending order of l (Steen *et al.* 2019). Figures 14(*a*,*b*) show two standard spectral orderings equivalent to the two standard PTs, which arise from the breaking of spectral degeneracy. For free semi-drops satisfying (1.1), modes are sorted in ascending order of k, but cannot be sorted by l due to the spectral degeneracy. As described above, the CL pinning, varying α or exerting gravity leads to the spectral splitting, so that modes with the same k can be sorted by l. For example, exerting low gravity (e.g. $Bo = 0.3$) to free semi-drops allows modes to be ordered in ascending order of l (see figure 13), and still maintains the ascending order of k, as shown in figure 14(*a*). Likewise, the CL pinning or slightly raising contact angle

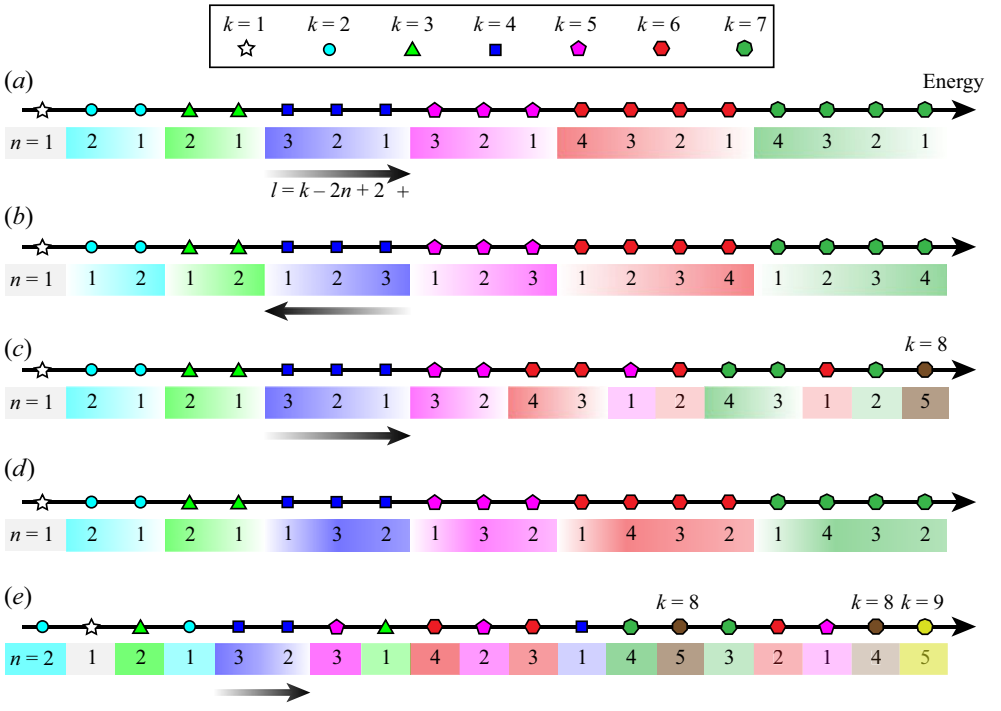

Figure 14. Spectral ordering of the first 19 modes. (*a*,*b*) In the two standard orderings (equivalent to the standard PTs proposed by Steen *et al.* 2019), modes are first sorted in ascending order of k, and then modes with the same k are sorted in (*a*) ascending or (*b*) descending order of l. (*c*–*e*) Three non-standard spectral orderings with irregularities arise from the breaking of the order of (*c*,*e*) k or (*d*) l.

(e.g. $\alpha = 91^\circ$) for free semi-drops can also result in the same standard spectral ordering (Steen *et al.* 2019). Similarly, the other standard spectral ordering in figure 14(*b*) can be generated by slightly lowering α or exerting opposite low gravity for free semi-drops, where modes with the same k are in descending order of l.

Figures 14(*c*–*e*) show several non-standard spectral orderings with irregularities when the order of l or k is broken. Exerting higher gravity, the order of k of few modes can be broken, e.g. $\lambda_{[k=6,l=0]} < \lambda_{[5,5]}$ for $Bo = 1$ shown in figure 14(*c*), while the order of l still holds. For the extreme case of a drop with $Bo = Bo_{max} \simeq 2.9$, $R = 1$ and a pinned CL, the order of k can even be completely broken (figure 14*e*). Figure 14(*d*) shows the breaking of the order of l, where the contact angle and gravity of free semi-drops are both changed (e.g. $\alpha = 85^\circ$ and $Bo = 0.3$). This is because lowering the contact angle and exerting gravity have opposite effects on the order of l, the competition of which breaks the order of l. In summary, gravity can also produce the same spectral orderings as in gravity-free cases (Steen *et al.* 2019), which provides an alternative to controlling the spectral ordering without varying contact angle.

4. Summary and conclusions

This paper is concerned with the static and dynamic stability of pendant drops, with attention to their relationship and the effects of gravity. Regarding static stability, the stability limits for volume and pressure disturbances (axisymmetric) correspond to the maximum volume (Bo_{max}) and maximum pressure, respectively (Padday & Pitt 1973).

We restrict our study to volume disturbances. Pendant drops can be v-unstable (to volume disturbances) due to the destabilisation of gravity, while gravity-free drops are always v-stable. For non-axisymmetric perturbations, drops with free CLs are marginally stable due to their horizontal translational invariance, whereas pinned ones are stable. The linear dynamic stability is then investigated numerically by the BE model (Zhang *et al.* 2023). Good agreement with experimental values of DePaoli *et al.* (1992) is found. Results show that the maximum drop (with Bo_{max}) that is marginally v-stable has a zero frequency mode $\{2, 0\}$ (figures 7, 9 and 12), as expected from the PM theory. Another zero frequency mode $\{1, 1\}$ is also observed, consistent with the prediction by the boundary parameter comparison approach, which suggests that pendant drops with free CLs are marginally stable to non-axisymmetric perturbations. This shows the high accuracy of our results and, in turn, validates the BE model. Interestingly, there are sharp changes in frequency near Bo_{max} (figures 9 and 14), which may lead to inaccurate theoretical predictions due to the high sensitivity of frequency on Bo. Therefore, we recommend avoiding experiments on pendant drops that are close to marginally v-stable for more accurate frequency predictions.

Our subsequent analysis endeavours to examine the effect of gravity on the frequency spectrum, where the natural frequencies are shifted upwards or downwards by gravity depending on the control parameters (α, Bo) or (R, Bo) and CL condition. There are three types of contour diagrams (I, II and T) of shift factors $S^f(\alpha, Bo)$ showing how gravity affects the frequency spectrum for free CLs, whereas there are only two types (A and B) of $S^p(R, Bo)$ diagrams for pinned CLs (figure 10). For instance, the frequencies of the zonal modes (type I) with free CLs are shifted upwards (downwards) at small (large) contact angles, whereas the frequencies of the zonal modes (type B) with pinned CLs are always shifted downwards. Subsequently, these types are categorised according to the modal pair $\{n, l\}$. Generally, modes with large n and small l more likely have diagrams of types I and B, whereas modes with small n and large l tend to types II and A (figure 11). As a result of frequency shifts, gravity, similar to CL pinning (Lyubimov *et al.* 2006) and varying α (Bostwick & Steen 2014), breaks the symmetry of the free semi-drop inherited from the RL spectrum, leading to the splitting of degenerate frequencies (1.1) (figure 13) and various spectral orderings (figure 14). In particular, gravity can also lead to two standard PTs proposed by Steen *et al.* (2019), which provides an alternative to controlling the spectral ordering without varying contact angle.

This work on pendant drops complements the study of the effects of gravity on the frequency spectrum of partially wetting drops on a plane. In most cases, the effects of gravity on pendant drops are opposite to those of gravity-flattened sessile drops (Zhang *et al.* 2023). Two notable features are the zero frequency $\{2, 0\}$ mode, which determines the stability limit, and the sharp frequency changes that occur as approaching the stability limit. Besides, our results confirm that the static stability of pendant drops can be recovered by letting $\lambda_{2,0} = 0$ in the dynamic stability, and the critical conditions for static and dynamic stability are essentially identical.

Funding. We are grateful for the support of the National Natural Science Foundation of China (grant nos 12102426, 11972170) and the China Postdoctoral Science Foundation (grant no. 2021M693080).

Declaration of interests. The authors report no conflict of interest.

Author ORCIDs.
Fei Zhang https://orcid.org/0000-0003-2087-0487;
Xinping Zhou https://orcid.org/0000-0001-6340-5273.

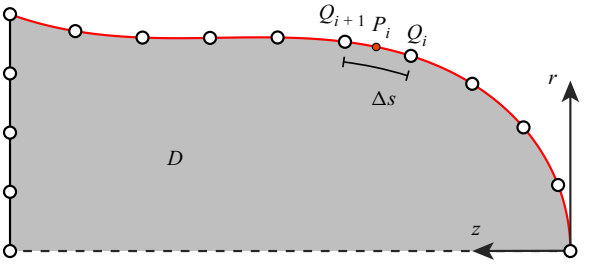

Figure 15. Schematic diagram of a uniformly discretised boundary ∂D. There are N uniform BEs for the liquid surface (red line), and M uniform BEs for the solid surface (black solid line). In each element, the midpoint P is employed as the collocation point, and the nodes Q located at both ends define the element shape.

Appendix A

The adoption of the BE method for solving functional eigenvalue problems has evolved into a well-established procedure (see e.g. Ebrahimian *et al.* 2013, 2015; Zhang *et al.* 2023). Thus we provide only a concise outline of the fundamental steps for constructing the BE model, as follows.

(i) For the discretised boundary ∂D shown in figure 15, the standard formulation (e.g. Pozrikidis 2002) of the BE method for the Laplace equation (2.12*a*) yields the following discrete matrix form (Zhang *et al.* 2023):

$$\boldsymbol{K}^l\boldsymbol{\phi}^* = \boldsymbol{H}^l\boldsymbol{\phi}, \quad l = 0, 1, \ldots, \tag{A1}$$

where $\boldsymbol{\phi}$ and $\boldsymbol{\phi}^*$ represent the values of the potential ϕ and its normal derivative $\partial\phi/\partial n$ at the collocation points P, respectively. Here, the influence matrices $\boldsymbol{K}^l$ and $\boldsymbol{H}^l$ for different l depend only on the shape of the boundary ∂D. By distinguishing the boundary ∂D into the solid ∂D^s and liquid ∂D^f surfaces (i.e. $\boldsymbol{\phi} = \begin{bmatrix}\boldsymbol{\phi}_L & \boldsymbol{\phi}_S\end{bmatrix}^{\mathrm{T}}$ and $\boldsymbol{\phi}^* = \begin{bmatrix}\boldsymbol{\phi}_L^* & \boldsymbol{\phi}_S^*\end{bmatrix}^{\mathrm{T}}$) and applying the no-penetration condition (2.12*b*) (i.e. $\boldsymbol{\phi}_S^* = 0$) to (A1), we have

$$\left[\boldsymbol{H}^l_{1,2}\left(\boldsymbol{H}^l_{2,2}\right)^{-1}\boldsymbol{K}^l_{2,1} - \boldsymbol{K}^l_{1,1}\right]\boldsymbol{\phi}_L^* = \left[\boldsymbol{H}^l_{1,2}\left(\boldsymbol{H}^l_{2,2}\right)^{-1}\boldsymbol{H}^l_{2,1} - \boldsymbol{H}^l_{1,1}\right]\boldsymbol{\phi}_L, \tag{A2}$$

where the subscripts S and L indicate the quantities measured at the solid and liquid surfaces, respectively, and the numerals in the subscripts of the influence matrices $\boldsymbol{K}$ and $\boldsymbol{H}$ indicate the positions of the submatrices.

(ii) Using the finite difference discretisation of the free-surface equation (2.12*c*) and then incorporating the free/pinned CL condition (2.12*e*) can lead to a system of linear equations (Ebrahimian *et al.* 2015; Zhang *et al.* 2023)

$$\tilde{\boldsymbol{K}}^l\boldsymbol{\phi}^* = -\lambda^2\boldsymbol{I}\boldsymbol{\phi}, \tag{A3}$$

where the influence matrix $\tilde{\boldsymbol{K}}^l$ depends on the form and order of the finite difference and the number N of BEs for the fluid surface, and $\boldsymbol{I}$ denotes the identity matrix.

(iii) Finally, combining (A2) and (A3) with the discretisation of the volume constraint (2.12*d*) yields matrix eigenvalue problems (Zhang *et al.* 2023)

$$\boldsymbol{X}\boldsymbol{\phi}_L^* = \lambda^2\boldsymbol{Y}\boldsymbol{\phi}_L^* \quad \text{for } l > 0, \tag{A4}$$

$$\boldsymbol{Z}^{\mathrm{T}}\boldsymbol{X}\boldsymbol{Z}\boldsymbol{v} = \lambda^2\boldsymbol{Z}^{\mathrm{T}}\boldsymbol{Y}\boldsymbol{Z}\boldsymbol{v} \quad \text{for } l = 0, \tag{A5}$$

with

$$\boldsymbol{X} = \left[\boldsymbol{H}^{l}_{1,1} - \boldsymbol{H}^{l}_{1,2}\left(\boldsymbol{H}^{l}_{2,2}\right)^{-1}\boldsymbol{H}^{l}_{2,1}\right]\tilde{\boldsymbol{K}}^{l}, \tag{A6a}$$

$$\boldsymbol{Y} = \left[\boldsymbol{H}^{l}_{1,2}\left(\boldsymbol{H}^{l}_{2,2}\right)^{-1}\boldsymbol{K}^{l}_{2,1} - \boldsymbol{K}^{l}_{1,1}\right], \tag{A6b}$$

$$\boldsymbol{\phi}^{*}_{L} = \boldsymbol{Z}\boldsymbol{v}, \tag{A6c}$$

where $\boldsymbol{Z}$ is the matrix whose columns span the null space $N(\boldsymbol{r}_L)$, and the vector $\boldsymbol{r}_L$ is a row consisting of the radii of collocation points P on the liquid surface. The matrix eigenvalue problems (A4) and (A5) can be solved effectively by various software tools (e.g. MATLAB), and their eigenvalues λ and eigenvectors $\boldsymbol{\phi}^{*}_{L}$ give the frequencies and mode shapes, respectively.

References

Basaran, O.A. 1992 Nonlinear oscillations of viscous liquid drops. *J. Fluid Mech.* **241**, 169–198.

Basaran, O.A. & DePaoli, D.W. 1994 Nonlinear oscillations of pendant drops. *Phys. Fluids* **6** (9), 2923–2943.

Bhattacharya, S. 2016 Interfacial wave dynamics of a drop with an embedded bubble. *Phys. Rev.* E **93** (2), 023119.

Bostwick, J.B. & Steen, P.H. 2009 Capillary oscillations of a constrained liquid drop. *Phys. Fluids* **21** (3), 032108.

Bostwick, J.B. & Steen, P.H. 2014 Dynamics of sessile drops. Part 1. Inviscid theory. *J. Fluid Mech.* **760**, 5–38.

Bostwick, J.B. & Steen, P.H. 2015 Stability of constrained capillary surfaces. *Annu. Rev. Fluid Mech.* **47**, 539–568.

Bostwick, J.B. & Steen, P.H. 2016 Response of driven sessile drops with contact-line dissipation. *Soft Matt.* **12** (43), 8919–8926.

Busse, F.H. 1984 Oscillations of a rotating liquid drop. *J. Fluid Mech.* **142**, 1–8.

Celestini, F. & Kofman, R. 2006 Vibration of submillimeter-size supported droplets. *Phys. Rev.* E **73** (4), 041602.

Chang, C.-H. & Franses, E.I. 1994 Dynamic tension behavior of aqueous octanol solutions under constant-area and pulsating-area conditions. *Chem. Engng Sci.* **49** (3), 313–325.

Chang, C.-T., Bostwick, J.B., Daniel, S. & Steen, P.H. 2015 Dynamics of sessile drops. Part 2. Experiment. *J. Fluid Mech.* **768**, 442–467.

Chang, C.-T., Bostwick, J.B., Steen, P.H. & Daniel, S. 2013 Substrate constraint modifies the Rayleigh spectrum of vibrating sessile drops. *Phys. Rev.* E **88** (2), 023015.

Concus, P. & Finn, R. 1979 The shape of a pendant liquid drop. *Phil. Trans. R. Soc. Lond.* A **292** (1391), 307–340.

Costalonga, M. & Brunet, P. 2020 Directional motion of vibrated sessile drops: a quantitative study. *Phys. Rev. Fluids* **5** (2), 023601.

Daly, B.J. 1969 Numerical study of the effect of surface tension on interface instability. *Phys. Fluids* **12** (7), 1340–1354.

Del Rio, O.I. & Neumann, A.W. 1997 Axisymmetric drop shape analysis: computational methods for the measurement of interfacial properties from the shape and dimensions of pendant and sessile drops. *J. Colloid Interface Sci.* **196** (2), 136–147.

DePaoli, D.W., Scott, T.C. & Basaran, O.A. 1992 Oscillation frequencies of droplets held pendant on a nozzle. *Sep. Sci. Technol.* **27** (15), 2071–2082.

Ding, D. & Bostwick, J.B. 2022*a* Oscillations of a partially wetting bubble. *J. Fluid Mech.* **945**, A24.

Ding, D. & Bostwick, J.B. 2022*b* Pressure modes of the oscillating sessile drop. *J. Fluid Mech.* **944**, R1.

Ding, H., Zhu, X., Gao, P. & Lu, X.-Y. 2018 Ratchet mechanism of drops climbing a vibrated oblique plate. *J. Fluid Mech.* **835**, R1.

Dubey, P., Roy, A. & Subramanian, G. 2022 Linear stability of a rotating liquid column revisited. *J. Fluid Mech.* **933**, A55.

EBRAHIMIAN, M., NOORIAN, M.A. & HADDADPOUR, H. 2013 A successive boundary element model for investigation of sloshing frequencies in axisymmetric multi baffled containers. *Engng Anal. Bound. Elem.* **37** (2), 383–392.

EBRAHIMIAN, M., NOORIAN, M.A. & HADDADPOUR, H. 2015 Free vibration sloshing analysis in axisymmetric baffled containers under low-gravity condition. *Microgravity Sci. Technol.* **27** (2), 97–106.

FENG, J.Q. 1992 The oscillations of a bubble moving in an inviscid fluid. *SIAM J. Appl. Maths* **52** (1), 1–14.

FENG, J.Q. & BEARD, K.V. 1991 Three-dimensional oscillation characteristics of electrostatically deformed drops. *J. Fluid Mech.* **227**, 429–447.

FINN, R. 1986 *Equilibrium Capillary Surfaces*. Springer.

GAÑÁN, A.M. 1991 Oscillations of liquid captive rotating drops. *J. Fluid Mech.* **226**, 63–89.

GAÑÁN, A.M. & BARRERO, A. 1990 Free oscillations of liquid captive drops. *Microgravity Sci. Technol.* **3**, 70–86.

GULEC, S., YADAV, S., DAS, R., BHAVE, V. & TADMOR, R. 2019 The influence of gravity on contact angle and circumference of sessile and pendant drops has a crucial historic aspect. *Langmuir* **35** (16), 5435–5441.

HAEFNER, S., BENZAQUEN, M., BÄUMCHEN, O., SALEZ, T., PETERS, R., MCGRAW, J.D., JACOBS, K., RAPHAËL, E. & DALNOKI-VERESS, K. 2015 Influence of slip on the Plateau–Rayleigh instability on a fibre. *Nat. Commun.* **6**, 7409.

HENDERSON, D.M., PRITCHARD, W.G. & SMOLKA, L.B. 1997 On the pinch-off of a pendant drop of viscous fluid. *Phys. Fluids* **9** (11), 3188–3200.

IBRAHIM, R.A. 2005 *Liquid Sloshing Dynamics: Theory and Applications*. Cambridge University Press.

KUMAR, K. 1996 Linear theory of Faraday instability in viscous liquids. *Proc. Math. Phys. Engng* **452** (1948), 1113–1126.

KUMAR, K. & TUCKERMAN, L.S. 1994 Parametric instability of the interface between two fluids. *J. Fluid Mech.* **279**, 49–68.

LAMB, H. 1932 *Hydrodynamics*. Cambridge University Press.

LOWRY, B.J. & STEEN, P.H. 1995 Capillary surfaces: stability from families of equilibria with application to the liquid bridge. *Proc. R. Soc. Lond.* A **449** (1937), 411–439.

LYUBIMOV, D.V., LYUBIMOVA, T.P. & SHKLYAEV, S.V. 2004 Non-axisymmetric oscillations of a hemispherical drop. *Fluid Dyn.* **39** (6), 851–862.

LYUBIMOV, D.V., LYUBIMOVA, T.P. & SHKLYAEV, S.V. 2006 Behavior of a drop on an oscillating solid plate. *Phys. Fluids* **18** (1), 012101.

MADDOCKS, J.H. 1987 Stability and folds. *Arch. Rat. Mech. Anal.* **99** (4), 301–328.

MARINOV, P. 2012 Stability of capillary surfaces with planar boundary in the absence of gravity. *Pac. J. Appl. Maths* **255** (1), 177–190.

MCCRANEY, J., KERN, V., BOSTWICK, J.B., DANIEL, S. & STEEN, P.H. 2022 Oscillations of drops with mobile contact lines on the International Space Station: elucidation of terrestrial inertial droplet spreading. *Phys. Rev. Lett.* **129** (8), 084501.

MICHAEL, D.H. 1981 Meniscus stability. *Annu. Rev. Fluid Mech.* **13** (1), 189–216.

MOLLOT, D.J., TSAMOPOULOS, J., CHEN, T.-Y. & ASHGRIZ, N. 1993 Nonlinear dynamics of capillary bridges: experiments. *J. Fluid Mech.* **255**, 411–435.

MONTANERO, J.M. & PONCE-TORRES, A. 2020 Review on the dynamics of isothermal liquid bridges. *Appl. Mech. Rev.* **72** (1), 010803.

MYSHKIS, A.D., BABSKII, V.G., KOPACHEVSKII, N.D., SLOBOZHANIN, L.A. & TYUPTSOV, A.D. 1987 *Low-Gravity Fluid Mechanics*. Springer.

NOBLIN, X., BUGUIN, A. & BROCHARD-WYART, F. 2004 Vibrated sessile drops: transition between pinned and mobile contact line oscillations. *Eur. Phys. J.* E **14** (4), 395–404.

NOBLIN, X., BUGUIN, A. & BROCHARD-WYART, F. 2009 Vibrations of sessile drops. *Eur. Phys.* J.*: Spec. Top.* **166** (1), 7–10.

PADDAY, J.F. 1971 The profiles of axially symmetric menisci. *Phil. Trans. R. Soc. Lond.* A **269** (1197), 265–293.

PADDAY, J.F. & PITT, A. 1972 Axisymmetric meniscus profiles. *J. Colloid Interface Sci.* **38** (2), 323–334.

PADDAY, J.F. & PITT, A.R. 1973 The stability of axisymmetric menisci. *Phil. Trans. R. Soc. Lond.* A **275** (1253), 489–528.

PARKINSON, L.M. & PHAN, C.M. 2018 Natural vibration of an aqueous pendant drop. *Exp. Therm. Fluid Sci.* **90**, 48–54.

PEREZ, M., BRECHET, Y., SALVO, L., PAPOULAR, M. & SUERY, M. 1999 Oscillation of liquid drops under gravity: influence of shape on the resonance frequency. *Eur. Phys. Lett.* **47** (2), 189–195.

PHAM, C.-T., PERRARD, S. & LE DOUDIC, G. 2020 Surface waves along liquid cylinders. Part 1. Stabilising effect of gravity on the Plateau–Rayleigh instability. *J. Fluid Mech.* **891**, A8.

PITTS, E. 1974 The stability of pendent liquid drops. Part 2. Axial symmetry. *J. Fluid Mech.* **63** (3), 487–508.
PLATEAU, J.A.F. 1873 *Statique expérimentale et théorique des liquides soumis aux seules forces moléculaires*, vol. 2. Gauthier-Villars.
POZRIKIDIS, C. 2002 *A Practical Guide to Boundary Element Methods with the Software Library BEMLIB*. CRC.
POZRIKIDIS, C. 2012 Stability of sessile and pendant liquid drops. *J. Engng Maths* **72** (1), 1–20.
RAYLEIGH, LORD 1878 On the instability of jets. *Proc. Lond. Math. Soc.* **1** (1), 4–13.
RAYLEIGH, LORD 1879 On the capillary phenomena of jets. *Proc. R. Soc. Lond.* **29** (196–199), 71–97.
SAKAKEENY, J., DESHPANDE, C., DEB, S., ALVARADO, J.L. & LING, Y. 2021 A model to predict the oscillation frequency for drops pinned on a vertical planar surface. *J. Fluid Mech.* **928**, A28.
SAKAKEENY, J. & LING, Y. 2020 Natural oscillations of a sessile drop on flat surfaces with mobile contact lines. *Phys. Rev. Fluids* **5** (12), 123604.
SAKAKEENY, J. & LING, Y. 2021 Numerical study of natural oscillations of supported drops with free and pinned contact lines. *Phys. Fluids* **33** (6), 062109.
SCASE, M.M. & HILL, R.J.A. 2018 Centrifugally forced Rayleigh–Taylor instability. *J. Fluid Mech.* **852**, 543–577.
SCHULKES, R.M.S.M. 1994 The evolution and bifurcation of a pendant drop. *J. Fluid Mech.* **278**, 83–100.
SHARMA, S. & WILSON, D.I. 2021 On a toroidal method to solve the sessile-drop oscillation problem. *J. Fluid Mech.* **919**, A39.
SHI, T. & APFEL, R.E. 1995 Oscillations of a deformed liquid drop in an acoustic field. *Phys. Fluids* **7** (7), 1545–1552.
SIEKMANN, J. & SCHILLING, U. 1989 On the vibrations of an inviscid liquid droplet contacting a solid wall in a low-gravity environment. *Appl. Microgravity Technol.* **2**, 17–26.
STEEN, P.H., CHANG, C.-T. & BOSTWICK, J.B. 2019 Droplet motions fill a periodic table. *Proc. Natl Acad. Sci. USA* **116** (11), 4849–4854.
STRANI, M. & SABETTA, F. 1984 Free vibrations of a drop in partial contact with a solid support. *J. Fluid Mech.* **141**, 233–247.
SUMANASEKARA, U.R. & BHATTACHARYA, S. 2017 Detailed finer features in spectra of interfacial waves for characterization of a bubble-laden drop. *J. Fluid Mech.* **831**, 698–718.
SUMESH, P.T. & GOVINDARAJAN, R. 2010 The possible equilibrium shapes of static pendant drops. *J. Chem. Phys.* **133** (14), 144707.
TEMPERTON, R.H., SMITH, M.I. & SHARP, J.S. 2015 Mechanical vibrations of pendant liquid droplets. *Eur. Phys. J.* E **38**, 79.
TRINH, E., ZWERN, A. & WANG, T.G. 1982 An experimental study of small-amplitude drop oscillations in immiscible liquid systems. *J. Fluid Mech.* **115**, 453–474.
TSAMOPOULOS, J.A. & BROWN, R.A. 1983 Nonlinear oscillations of inviscid drops and bubbles. *J. Fluid Mech.* **127**, 519–537.
WANG, T.G., ANILKUMAR, A.V. & LEE, C.P. 1996 Oscillations of liquid drops: results from USML-1 experiments in space. *J. Fluid Mech.* **308**, 1–14.
WENTE, H. 1980 The symmetry of sessile and pendent drops. *Pac. J. Appl. Maths* **88** (2), 387–397.
YARIV, E. 2022 Shape of sessile drops at small contact angles. *J. Fluid Mech.* **950**, R4.
YOSHIYASU, N., MATSUDA, K. & TAKAKI, R. 1996 Self-induced vibration of a water drop placed on an oscillating plate. *J. Phys. Soc. Japan* **65** (7), 2068–2071.
ZHANG, F. & ZHOU, X. 2020 General exotic capillary tubes. *J. Fluid Mech.* **885**, A1.
ZHANG, F., ZHOU, X. & DING, H. 2023 Effects of gravity on natural oscillations of sessile drops. *J. Fluid Mech.* **962**, A10.